

# MAGNETICALLY-MODULATED HEAT TRANSPORT IN A GLOBAL SIMULATION OF SOLAR MAGNETO-CONVECTION

JEAN-FRANCOIS COSSETTE

Laboratory for Atmospheric and Space Physics, Campus Box 600, University of Colorado, Boulder, CO 80303 USA;  
Jean-Francois.Cossette@lasp.colorado.edu

PAUL CHARBONNEAU

Département de Physique, Université de Montréal, C.P. 6128, Succ. Centre-Ville, Montréal, QC H3C 3J7, Canada;  
paulchar@astro.umontreal.ca

PIOTR K. SMOLARKIEWICZ

European Centre for Medium-Range Weather Forecasts, Reading, RG2 9AX, UK; smolar@ecmwf.int

MARK P. RAST

Department of Astrophysical and Planetary Sciences, Laboratory for Atmospheric and Space Physics, Campus Box 391, University of Colorado, Boulder, CO 80303 USA; Mark.Rast@lasp.colorado.edu

*Draft version February 13, 2017*

## ABSTRACT

We present results from a global MHD simulation of solar convection in which the heat transported by convective flows varies in-phase with the total magnetic energy. The purely random initial magnetic field specified in this experiment develops into a well organized large-scale antisymmetric component undergoing hemispherically synchronized polarity reversals on a 40yr period. A key feature of the simulation is the use of a Newtonian cooling term in the entropy equation to maintain a convectively unstable stratification and drive convection, as opposed to the specification of heating and cooling terms at the bottom and top boundaries. When taken together, the solar-like magnetic cycle and the convective heat flux signature suggest that a cyclic modulation of the large-scale heat-carrying convective flows could be operating inside the real Sun. We carry out an analysis of the entropy and momentum equations to uncover the physical mechanism responsible for the enhanced heat transport. The analysis suggests that the modulation is caused by a magnetic tension imbalance inside upflows and downflows, which perturbs their respective contributions to heat transport in such a way as to enhance the total convective heat flux at cycle maximum. Potential consequences of the heat transport modulation for solar irradiance variability are briefly discussed.

*Subject headings:* Solar convection, magnetohydrodynamics, solar irradiance

## 1. INTRODUCTION

The Sun's magnetic field is at the origin of all phenomena collectively known as 'solar activity', with the 11-yr solar activity cycle being its most conspicuous manifestation. The latter regulates the myriad of events driving space weather, such as flares and coronal mass ejections, as well as variations in the solar radiative output. State-of-the-art numerical simulations of global MHD convection are now capable of producing large-scale well-organized magnetic fields undergoing polarity reversals (Ghizaru et al. 2010; Käpylä et al. 2010; Racine et al. 2011; Brown et al. 2011; Käpylä et al. 2012; Masada et al. 2013; Nelson et al. 2013; Fan & Fang 2014; Augustson et al. 2015; Duarte et al. 2016; Guerrero et al. 2016). In addition to the insight they can offer on the mode of operation of the solar dynamo, such simulations may provide useful insights as to how cyclic magnetic activity impacts global thermodynamic structure and large-scale heat carrying convective motions. In particular, recent results from global MHD simulations of solar convection produced with the EULAG-MHD model achieve solar-like magnetic cycles in which the total enthalpy flux

varies in-phase with the total magnetic energy (Cossette et al. 2013). Together, the solar-like magnetic cycle and the enthalpy flux signature suggest that large-scale heat carrying convective motions inside the real Sun could be modulated in such a way as to enhance energy transport at cycle maximum.

Possible observational signatures of cycle-driven sub-photospheric alterations of the thermodynamical structure of the outer convective envelope have been sought by a variety of means. Spectroscopic measurements of line-depth ratios identifying surface temperature changes that are expected to be free from the influence of faculae and plage reveal that those variations are either small or non-existent (Gray & Livingston 1997; Livingston & Wallace 2003). Some solar limb intensity measurements suggest a brightness enhancement at high latitudes, which could be thermal in origin, and not due to the presence of magnetic structures on the disk (e.g. see Rast et al. (2008) and the references therein). However, it is unclear whether this polar enhancement correlates with solar activity (Woodard & Libbrecht 2003). Variations of the solar diameter are expected to be a direct consequence of structural changes induced by mag-

netic activity, and their possible contribution to long-term variations of total solar irradiance (TSI) has been suggested (Li et al. 2003; Rozelot et al. 2004; Sofia & Li 2006). Space-based helioseismic measurements (Emilio et al. 2000; Antia 2003; Kuhn et al. 2004) set an upper limit of a few km on the change in solar radius from cycle minimum to cycle maximum, while ground-based observations yield conflicting results about the magnitude and phase of the change with the cycle (Thuillier et al. 2005).

So far, the best observational evidence for potential global structural changes related to solar activity remains the positive phase relationship between low  $l$  angular degree  $p$  mode oscillations frequency splittings and indicators of magnetic activity, including the 11-year TSI component, as inferred from helioseismology (Woodard & Noyes 1985; Woodard 1987; Bhatnagar et al. 1999).  $p$ -modes are acoustic waves confined to cavities with sizes determined by lower and upper turning points at which pressure wave fronts are refracted back into the cavity. Low  $l$  modes have a lower turning point located deep within the interior, and could reflect the impact of the deep seated dynamo on the thermodynamic structure. However, the strong increase of the observed frequency modulation's amplitude with the mode's frequency instead suggests an origin close to the surface. This is due to the fact that low frequency modes have their upper turning point located deeper inside the interior (Libbrecht & Woodard 1990; Chaplin et al. 2001). Noteworthy, Fletcher et al. (2010) have reported the existence of a quasi-biennial signal located significantly deeper than the source of the 11 yr signal, which could be dynamo related (see, e.g., Beaudoin et al. 2016).

Despite the inherent difficulties associated with their direct measurement, deep-seated, magnetically-driven structural changes continue to be invoked as possible contributors to the observed variability in TSI, especially with regards to possible secular changes unfolding on timescales much longer than the primary magnetic cycle. An analogy based on the assumption that turbulent fluid motions behave as diffusion implies that a deep-seated decadal modulation of convective heat transport is unlikely to affect the energy output at the solar surface as a result of the convection zone's huge thermal relaxation time of  $\mathcal{O}(10^5)$  yr (Foukal 1987; Spruit 2000; Foukal et al. 2006). On the other hand, such a diffusive approximation may be ill-suited to the highly turbulent regime characterizing the solar interior. In particular, convective plumes generated at the model boundaries can transport their thermal energy content non-locally over several pressure scale heights before releasing it into the surrounding fluid (e.g. Stein & Nordlund 1989; Nordlund et al. 2009). The local heat flux is then no longer set by the local temperature gradient, which restricts the applicability of a purely diffusive approach substantially complicate the following discussion (e.g. Spruit 1997).

Global MHD convection simulations generating regular cycles represent an avenue towards quantifying such effects. While none of the aforementioned simulations operate in a dissipative regime close to solar interior conditions, there is some experimental (numerical) evidence that simulation results are scalable at least to some extent (Yadav et al. 2013). Moreover, with the magnetic energy density of the large-scale cycling magnetic field reaching many percents of equipartition with the tur-

bulent convective motions in some of these simulations, magnetically-driven alteration of convection and/or temperature gradients is expected, and has indeed been detected in some experiments (Cossette et al. 2013; Käpylä et al. 2013; Augustson et al. 2015; Beaudoin et al. 2016).

In this paper we conduct a detailed analysis of the convective dynamo simulation reported in (Cossette et al. 2013) to uncover the physical mechanism at the origin of the measured convective flux modulation. The paper is organized as follows: The model formulation and computational setup of our experiment are described in section 2. In section 3 we explore the flow morphology and thermodynamic structure in relationship to the convective heat flux modulation with cyclic magnetic field. The role of the thermal forcings of the system is assessed in section 4 and the impact of dynamical drivers on heat transport is addressed in section 5. Estimates of the total irradiance change induced by the cyclic modulation are computed in section 6 based on the diffusion approximation. Remarks and a discussion are included in section 7, which concludes the paper.

## 2. MODEL

We simulate solar magneto-convection by solving the Lipps & Hemler (Lipps & Hemler 1982) version of the anelastic MHD Navier-Stokes equations governing the evolution of momentum, entropy perturbations and magnetic induction for an electrically-conducting fluid inside a thick, gravitationally-stratified rotating spherical shell ranging from  $r_b = 0.61R_\odot$  to  $r_t = 0.962R_\odot$  in solar radius:

$$\frac{D\mathbf{u}}{Dt} = -\nabla\varphi' - \mathbf{g}\frac{\Theta'}{\Theta_0} + 2\mathbf{u} \times \boldsymbol{\Omega} + \frac{1}{\mu\rho_0}\mathbf{B} \cdot \nabla\mathbf{B} + \mathcal{D}_{\mathbf{u}}, \quad (1)$$

$$\frac{D\Theta'}{Dt} = -\mathbf{u} \cdot \nabla\Theta_a - \alpha\Theta' + \mathcal{D}_{\Theta}, \quad (2)$$

$$\frac{D\mathbf{B}}{Dt} = \mathbf{B} \cdot \nabla\mathbf{u} - \mathbf{B}\nabla \cdot \mathbf{u} + \mathcal{D}_{\mathbf{B}}, \quad (3)$$

$$\nabla \cdot (\rho_0\mathbf{u}) = 0, \quad (4)$$

$$\nabla \cdot \mathbf{B} = 0. \quad (5)$$

Here,  $\mathbf{u}$  and  $\mathbf{B}$  represent, respectively, the flow velocity and magnetic field vectors,  $\Theta$  is the potential temperature. The latter is equivalent to the specific entropy since  $ds = c_p d \ln \Theta$ , with  $c_p$  the specific heat at constant pressure. The operators  $\dot{D}/Dt$  and  $\nabla$  have their usual meaning, so that  $D/Dt := \partial/\partial t + \mathbf{u} \cdot \nabla$ . Likewise, symbols  $\boldsymbol{\Omega}$  and  $\mu$  stand for, respectively, the angular velocity of the rotating reference frame and the magnetic permeability. On the right-hand-side (rhs) of the momentum equation (1),  $\varphi' \equiv p'/\rho_0$  is a density-normalized pressure perturbation, in which magnetic pressure and centrifugal forces have been subsumed. Subscripts 'o' and 'a' correspond, respectively, to the *reference* state and *ambient* state, defined in sections 2.1 and 2.2, respectively. Operators  $\mathcal{D}$  appearing on the rhs of each prognostic equation represent either vector or scalar Laplacians used for explicit viscous/magnetic dissipation and radiative heat diffusion/conduction. Primes on the right-hand-side (rhs) of the momentum (1) and entropy equations (2) denote perturbations  $\Phi' \equiv \{\mathbf{u}', \Theta', \varphi', \mathbf{B}'\} \equiv \Phi - \Phi_a$  with respect to the ambient state  $\Phi_a \equiv \{\mathbf{u}_a, \Theta_a, \varphi_a, \mathbf{B}_a\}$ . In

the potential temperature equation (2)  $\alpha$  is the inverse time scale of the Newtonian cooling, and

$$\mathcal{D}_\Theta = \mathcal{H}(\Theta') \equiv \frac{\Theta_o}{\rho_o T_o} \left[ \nabla \cdot \left( \kappa_r \rho_o \nabla T' \right) + \nabla \cdot \left( \kappa \frac{\rho_o T_o}{\Theta_o} \nabla \Theta' \right) \right], \quad (6)$$

where  $T' \equiv \Theta' T_o / \Theta_o$ , while  $\kappa_r$  and  $\kappa$  denote coefficients of radiative and thermal conductivity (cf. §1.2.5 in Charbonneau 2013). Notably, (6) excludes the heating due to viscous and Ohmic dissipation, as it is of minor importance for the scope of this paper (Charbonneau 2013, *ibid.*) but can substantially complicate the following discussion.

### 2.1. Reference state

Reference states are inherent in anelastic approximations, as they enable complexity reduction of the compressible Euler equations under gravity—by analytically filtering acoustic modes energetically insignificant for the problems addressed—while retaining the relevant physics (cf. footnote 3 in Christensen-Dalsgaard et al. 1996). A key role of the reference state is to uncouple a dominating hydrostatic balance, to justify linearizations required to achieve a physically-relevant complexity reduction. Otherwise, the reference state does not have to be unique nor represent the actual mean state of the system. The primary strength of established reference states is their generally recognized theoretical and practical validity.

The reference state used in our simulations is standard. It assumes an unmagnetized, rigidly rotating and isentropic plasma (i.e.  $\Theta_o = \text{const.}$ ) obeying the ideal gas law  $p_o = \rho_o R T_o$  and hydrostatic balance  $dp_o/dr = -\rho_o g$ , whereby

$$\frac{dT_o}{dr} \equiv \frac{dT}{dr} \Big|_{\text{ad}} = -\frac{g}{c_p}, \quad (7)$$

where  $R = k/(\bar{\mu} m_H)$ ,  $k$  is the Boltzmann constant,  $m_H$  is the mass of a proton,  $\bar{\mu}$  is the mean molecular weight, and the gravitational acceleration  $g(r) \equiv g_b (r_b/r)^2$ . The reference state profiles  $T_o(r)$  and  $\rho_o(r)$  are constructed by integrating (7) using values for the temperature  $T_b$ , potential temperature  $\Theta_o = T_b$ , density  $\rho_b$  and gravitational acceleration  $g_b$  at the base of the domain obtained from a solar structure model (Christensen-Dalsgaard et al. 1996).

### 2.2. Ambient state

The notion of ambient states is distinct. The utilization of an ambient state is justified by expediency and optional for any system of the governing equations. The role of ambient states is to enhance the efficacy of numerical simulation—e.g. by simplifying the design of the initial and boundary conditions—without resorting to linearization of the system. The key underlying assumption is that the ambient state is a particular solution of the governing problem, so that subtracting its own minimal set of PDEs from the governing equations can form a useful perturbational form of the governing system. In general, ambient states can be spatially and temporally variable to represent, e.g., thermally balanced large-scale steady flows in atmospheric models (Smolarkiewicz et al. 2001; Smolarkiewicz et al. 2014) or prescribe oceanic tidal motions (Warn-Varnas et al. 2007).

To derive a useful perturbational form of the governing equations (1) and (2), we consider a zonally and meridionally averaged temporal mean state  $\Phi^* \equiv \{\mathbf{u}^*, \Theta^*, \varphi^*, \mathbf{B}^*\}$ , hereafter referred to as the *mean solar-state*—a particular solution to the generic anelastic MHD equations

$$\frac{D\mathbf{u}}{Dt} = -\nabla \cdot \left( \frac{p - p_o}{\rho_o} \right) - \mathbf{g} \frac{\Theta - \Theta_o}{\Theta_o} + 2\mathbf{u} \times \boldsymbol{\Omega} + \frac{1}{\mu \rho_o} \mathbf{B} \cdot \nabla \mathbf{B} + \mathcal{D}_\mathbf{u}, \quad (8)$$

$$\frac{D\Theta}{Dt} = \frac{\Theta_o}{\rho_o T_o} \left[ \nabla \cdot \left( \kappa_r \rho_o \nabla T \right) + \nabla \cdot \left( \kappa \frac{\rho_o T_o}{\Theta_o} \nabla \Theta \right) \right] \quad (9)$$

together with (3)-(5), which are already in the generic form. Because we are interested in fluctuations  $\tilde{\Phi} \equiv \{\tilde{\mathbf{u}}, \tilde{\Theta}, \tilde{\varphi}, \tilde{\mathbf{B}}\} \equiv \Phi - \Phi^*$  about  $\Phi^*$  arising from flow turbulence and magnetism, the temporal mean is assumed over a period  $t^*$  much longer than the 11 yr solar cycle and much shorter than the Kelvin-Helmholtz time scale. This mean solar-state is built-up over the course of stellar evolution, during which nuclear burning and mixing change the composition and structure of the star, and reflects the hydrostatic and thermodynamic equilibrium characterizing the Sun. Although  $\Phi^*$  cannot be directly observed, it may be approximated as a global anelastic hydrostatic thermodynamic equilibrium consistent with helioseismically calibrated solar structural models. Given such a hypothetical state, we derive (1) and (2) by subtracting the spatially and temporally averaged momentum and entropy equations from their generic counterparts (8) and (9). Below we summarize the result of this procedure, while referring to Appendix A for details.

Performing the spatial and temporal average of (9) yields

$$0 = \mathcal{H}(\Theta^*) + \mathcal{H}^*, \quad (10)$$

where  $\mathcal{H}^*$  denotes the second term on the rhs of (44) in Appendix A that represents the divergence of the Reynolds heat flux formed from the product of radial velocity  $\tilde{u}_r$  and entropy  $\tilde{\Theta}$  perturbations about the mean solar-state, averaged spatially over longitude and latitude and temporally over  $t^*$  as defined by (41). The  $\mathcal{H}(\Theta^*)$  term on the rhs of (10) incorporates radiative heating at the base of the convection zone and cooling at the model top, while  $\mathcal{H}^*$  reflects the balancing action of Reynolds fluxes implied by the thermodynamic equilibrium. Subtracting (10) from the conservative form of the generic entropy equation (9) leads to the perturbational form

$$\frac{D\tilde{\Theta}}{Dt} = -\mathbf{u} \cdot \nabla \Theta^* + \mathcal{H}(\tilde{\Theta}) - \mathcal{H}^*. \quad (11)$$

Similarly, performing the spatial and temporal average of (1) leads to the conservative perturbational form (49) and, thus, its Lagrangian equivalent

$$\frac{D\mathbf{u}}{Dt} = -\nabla \cdot \left( \frac{p - (p^* + \psi^*)}{\rho_o} \right) - \rho_o \mathbf{g} \frac{\tilde{\Theta}}{\Theta_o} + 2\mathbf{u} \times \boldsymbol{\Omega} + \frac{1}{\mu \rho_o} \nabla \cdot (\mathbf{B}\mathbf{B}) + \mathcal{D}_\mathbf{u}, \quad (12)$$

where  $\psi^*$ , defined in (47), accounts for Reynolds and Maxwell fluxes due to the correlations of fluctuating rad-

dial velocity and radial magnetic field components associated with the mean-solar-state equilibrium.

The equations (10)-(12) are instructive for the interpretation and design of the ambient state. Given the availability of  $\Theta^*$ , (12) can be straightforwardly integrated, because  $p' = p - (p^* + \psi^*)$  is determined from the elliptic boundary value problem implied by (4) and suitable boundary conditions (Smolarkiewicz & Charbonneau 2013). Consequently, we identify the ambient state as

$$\Phi_a = \{\mathbf{u}_a, \Theta_a, p_a, \mathbf{B}_a\} \equiv \{\mathbf{0}, \Theta^*, p^* + \psi^*, \mathbf{0}\}, \quad (13)$$

upon which,  $\mathbf{u}' \equiv \mathbf{u}$  and  $\mathbf{B}' \equiv \mathbf{B}$ , while  $\Theta' = \tilde{\Theta}$  and  $\varphi' = (p - p_a)/\rho_0$ . Although  $p_a$  is not required to solve for the perturbations, when needed it can be evaluated from the hydrostatic relation (48). Similarly,  $\mathcal{H}^*$  can be diagnosed from (10). The equilibrium assumption underlying (10)-(13) provides global constraints (10) and (48) on the eddy heat and momentum transfer. These constraints are consistent with the governing PDEs and the mean entropy profile. While deriving (10) we considered actual coefficients of molecular viscosity and radiative/thermal conductivity, envisioning a hypothetical direct numerical simulation. However, this same procedure could be applied to the generic anelastic equations (8) and (9) supplied with an explicit subgrid-scale turbulence model for large-eddy simulations (LES). Then, the global constraint implied by the mean equilibrium would also include fluctuations due to the intermittent eddy viscosity and diffusion.

The importance of modeling unresolved eddy fluxes is widely recognized. Standardly, numerical models of solar magneto-convection rely on scale-selective Fickian fluxes with eddy viscosity and diffusion. The computational (nonlinear) stability of EULAG simulations relies on the non-oscillatory numerics (Smolarkiewicz & Charbonneau 2013) that implies an implicit subgrid-scale model with a proven property of scale selective dissipation in the spirit of LES turbulence closures (Domaradzki et al. 2003; Waite & Smolarkiewicz 2008; Strugarek et al. 2016). Similarly to explicit turbulence models, it regularizes spectral energy transfer in small scales, while resorting to minimized implicit diffusion (cf. Fig. 5 in Strugarek et al. 2016). Such diffusion does not necessarily assure the control of mean equilibria, hence the role of the Newtonian cooling on the rhs of (2) is to do so, without compromising the low diffusivity of the implicit model. The Newtonian cooling is a natural choice (Farhat et al. 2015, 2016) for basic time-continuous data assimilation, and it forms an elementary case of the Kalman-Bucy filter (Krener 1980). The adopted approach is common in atmospheric and oceanic models addressing evolutionary fluctuations about large scale equilibria (Held & Suarez 1994; Smolarkiewicz et al. 2001; Grabowski & Smolarkiewicz 2002; Warn-Varnas et al. 2007) and has proven effective in previous global/Cartesian solar HD/MHD convection simulations (Ghizaru et al. 2010; Racine et al. 2011; Cossette et al. 2013; Guerrero et al. 2013, 2016; Strugarek et al. 2016; Cossette & Rast 2016).

Nevertheless, the true mean-solar state assumed in (10)-(13) is unavailable. Based on the phenomenology of the Sun, we approximate  $\Theta_a$  using a piecewise linear polytrope, which allows the specification of subadiabatic

and superadiabatic stratifications in the regions corresponding to the radiative interior ( $r \leq r_i$ ) and convection zone ( $r > r_i$ ), with  $r_i = 0.718$  the position of the interface; see Appendix B for details. For the time scale  $\tau = \alpha^{-1}$  of the Newtonian cooling, here  $\tau \sim \mathcal{O}(10^8)$  s is assumed. This scale is much longer than the typical turnover time of the largest convective cells, gives the most solar-like convective dynamo for the specified  $\Theta_a$ , and corresponds to the e-folding scale implied by the explicit eddy viscosity  $\mathcal{O}(10^8)$  m<sup>2</sup>s<sup>-1</sup>—representative of comparable solar simulations, (Strugarek et al. 2016)—for the Fourier modes with wavelengths  $\lambda \approx R_\odot$ .

### 2.3. Numerical approximations and boundary conditions

To carry out the integration of (1)-(3) in time and space, we use the MHD-extended version of the EULAG model predominantly used in atmospheric and climate research (Prusa et al. 2008). The extended version is a general-purpose, high-performance HD/MHD code for simulating flows from micro to planetary and stellar scales. At the core of EULAG-MHD are semi-implicit, non-oscillatory forward-in-time (NFT) integrators, powered with the multidimensional positive-definite advection transport algorithm, MPDATA—a widely documented class of flux-form Eulerian NFT advection operators (see Smolarkiewicz 2006, for a review). It is this non-oscillatory property of MPDATA that allows to dispense with the explicit dissipative terms  $\mathcal{D}$  in (1)-(3) (Smolarkiewicz & Prusa 2002). The MPDATA-based NFT schemes adapt diffusion to extreme gradients of the advected quantity, thereby minimizing the effect of numerical dissipation at any given resolution (Piotrowski et al. 2009). Experiments carried out with EULAG can use any combination of explicit and implicit dissipative treatments. In particular, they can be run entirely as explicitly-inviscid implicit large-eddy-simulations (ILES), whereby all dissipation is delegated to the truncation terms of MPDATA (Margolin et al. 2006). On the strong scale dependence of the effective dissipation in these simulations, see the spectral-energy-budget analysis of Strugarek et al. (2016). A relevant signature of the EULAG integrators is the trapezoidal-rule representation of the essential forcings on the rhs of (1)-(3), which in the context of (2) prevents dilution of  $\Theta_a$  by the diffusivity of advection (Smolarkiewicz et al. 2001). In Appendix C we highlight the aspects of the NFT integrators for (1)-(3) that are important for the analysis presented in the remainder of this paper. For a detailed exposition of the numerical techniques used in EULAG-MHD, the interested reader is referred to Smolarkiewicz & Charbonneau (2013).

Boundary conditions at the bottom and top boundaries are stress-free and impermeable for the velocity, the magnetic field is forced to be radial, whereas the radial flux of potential temperature is set to zero. Discrete differentiation extends across the poles for all variables, with a flipping of sign for both longitudinal and meridional components of the differentiated vector fields.

### 3. MAGNETICALLY-MODULATED CONVECTION

The simulation that we consider is an extended version of the low resolution simulation reported in (Cossette et al. 2013) where only radiative diffusion is present ( $\kappa = 0$ ), and  $N_\phi \times N_\theta \times N_r = 128 \times 64 \times 47$ , where  $N_\phi$ ,  $N_\theta$  and

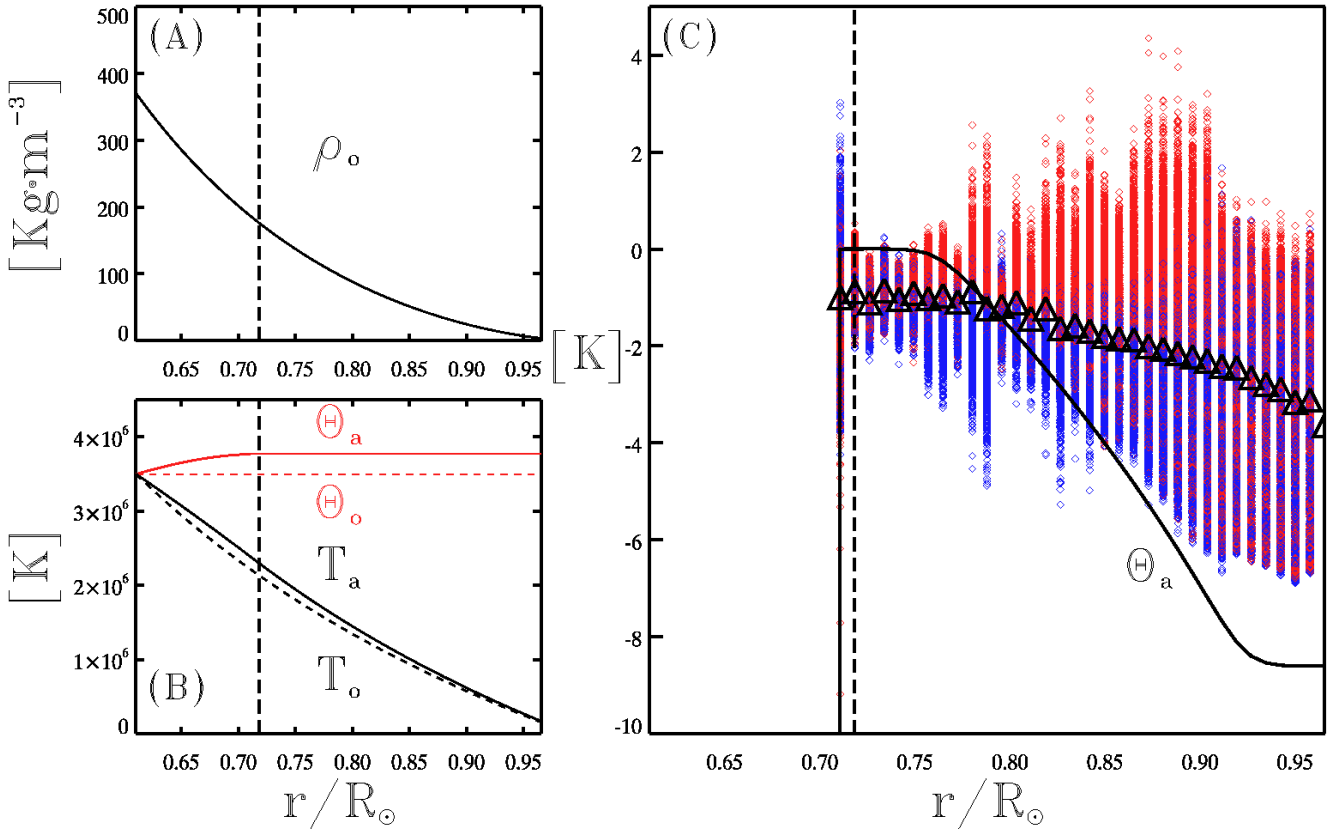


FIG. 1.— Reference state density profile (panel A) and profiles of the reference (dashed lines) and ambient (continuous lines) temperature and potential temperature (panel B). Panel (C) shows the variations of  $\Theta_a - \Theta_a(r_i)$  (black line) and  $\bar{\Theta} - \Theta_a(r_i)$  (black triangles) inside the bulk of the convection zone. Red and blue diamond symbols correspond to instantaneous values of the  $\Theta - \Theta_a(r_i)$  variation, respectively, in upflows and downflows. In each plot, a vertical straight line marks the location of the interface between the stable and unstable layers at  $r_i = 0.718R_\odot$ .

$N_r$  are the numbers of grid points in the azimuthal, latitudinal and radial directions. In (1) we set  $\mathcal{D}_u = 0$ , whereby all dissipation is treated implicitly (cf. section 2.3); whereas in (3)  $\mathcal{D}_B \equiv \eta \nabla^2 \mathbf{B}$ , with  $\eta = 10^6 \text{ m}^2 \cdot \text{s}^{-1}$  everywhere inside the domain. Figure 1 shows the relevant reference and ambient state profiles associated with polytropic indices  $m_s = 2.6$  and  $m_u = 1.4999945$ ; here  $T_a \approx T_o(\Theta_a/\Theta_o)$  is assumed. This choice of the parameters sets strongly subadiabatic and weakly superadiabatic ambient stratifications in the stable and unstable layers, respectively (cf. Appendix B). Specifically, this corresponds to a superadiabaticity parameter

$$\epsilon_a \equiv \frac{dT_a/dr - dT_o/dr}{dT_o/dr} = -\frac{H_T}{\Theta_o} \frac{d\Theta_a}{dr} \approx 10^{-6}, \quad (14)$$

in the bulk of the convection zone, which is consistent with the estimates inferred from solar structural models  $\epsilon \lesssim 10^{-4}$ , with  $H_T \equiv -(d \ln T_o / dr)^{-1}$  the temperature scale height (Miesch 2005). The simulation is initialized by adding a small random perturbation to the ambient state  $\Theta = \Theta_a + \Theta'$  and by specifying a low-amplitude random magnetic field subject to (5). Mixing by flow motions homogenizes entropy perturbations and tends to produce an adiabatic temperature profile. This effect is opposed by Newtonian cooling, which damps entropy perturbations  $\Theta'$  toward zero on the timescale  $\tau$  (defined by the end of §2.2). The mean potential temperature

profile  $\bar{\Theta}$  resulting from these two competing effects is slightly less superadiabatic than the ambient state, with  $\bar{\epsilon} \equiv -H_T/\Theta_o \partial \bar{\Theta} / \partial r \approx 1 - 5 \times 10^{-7}$  in the bulk of the unstable layer; see panel (C) in Fig. 1. Here,  $(\bar{\cdot})$  denotes the spatial average over a spherical surface and over the full temporal extent of the simulation, hereafter referred to as the *simulation mean*.

At mid/high latitudes inside the unstable layer the convection pattern is dominated by a network of broad upflows and cooler narrow downflow lanes (Fig. 2). This arrangement is typical of convection in a density-stratified environment and has been well documented by numerical simulations (Cattaneo et al. 1991; Brummell et al. 1996; Porter & Woodward 2000). Regions near the equator are marked by a pattern of north-south aligned convective cells (also known as ‘banana cells’), which are a feature of rotationally constrained convection (Miesch et al. 2000; Brun & Toomre 2002; Miesch et al. 2008). The velocity field is also characterized by a solar-like differential rotation with a fast equator and slow poles, as shown by previous analyses of similar simulations; e.g. see Fig. 2 of Beaudoin et al. (2013). This pattern is marked by isocontours of the angular velocity nearly parallel to the rotation axis, as opposed to those inferred from helioseismology (Thompson et al. 2003). The cylindrical shape of the angular velocity isocontours is a consequence of the Taylor-Proudman constraint on the rotating system,

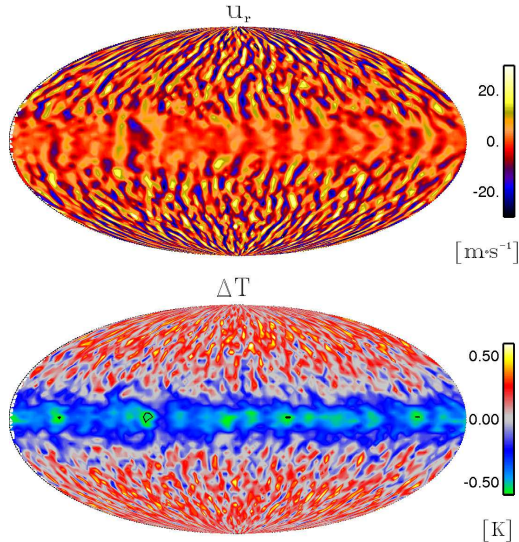


FIG. 2.— Mollweide projections of the radial velocity and temperature perturbation with respect to the simulation mean  $\bar{T}$  at  $r/R_\odot = 0.90$ .

and is a characteristic that is common to this type of simulations (Miesch et al. 2000; Elliott & Smolarkiewicz 2002; Brun et al. 2004; Miesch et al. 2006; Guerrero et al. 2013).

The simulation is characterized by the build-up of a well-organized large-scale magnetic field undergoing cyclic hemispheric polarity reversals on a regular 40 yr cadence. Figure 3 shows the evolution over the course of a half magnetic cycle of the toroidal magnetic field component and its zonal average

$$\langle B_\phi \rangle(\theta, r, t) \equiv \frac{1}{2\pi} \int_0^{2\pi} B_\phi(\phi, \theta, r, t) d\phi. \quad (15)$$

At cycle maximum the field is antisymmetric with respect to the equator (i.e. of the opposite sign in each hemisphere), is concentrated at mid/high latitudes and near the core-envelope interface (here denoted by the dashed line), whereas at minimum the average field intensity drops significantly and field polarity in each hemisphere reverses, with the large-scale field component building-up again at maximum. Magnetic field lines reveal the presence of a well-organized toroidal flux system (Fig. 4) having the intensity of a few Kilogauss (denoted blue), which correspond to the high-latitude toroidal field concentrations identified in figure 3.

The evolution of the longitudinally-averaged toroidal and radial magnetic field components is shown in Fig. 5. Panels (A) and (B) show that the mean toroidal field strength peaks at mid/high latitudes ( $\approx \theta = 50^\circ$ ) and immediately beneath the core-envelope interface (panel C), where the zonally-aligned antisymmetric wreaths are found to be concentrated (cf. Fig. 3). Each wreath undergoes hemispheric polarity reversals at an average rate of  $0.025 \text{ yr}^{-1}$  (Passos & Charbonneau 2014). These properties turn out to be essential ingredients of the interface dynamo, in which the build-up and storage of magnetic flux tubes inside the stable layer, and their subsequent destabilization and buoyant rise up to the surface leads to the formation of bipolar active regions obeying Hale's

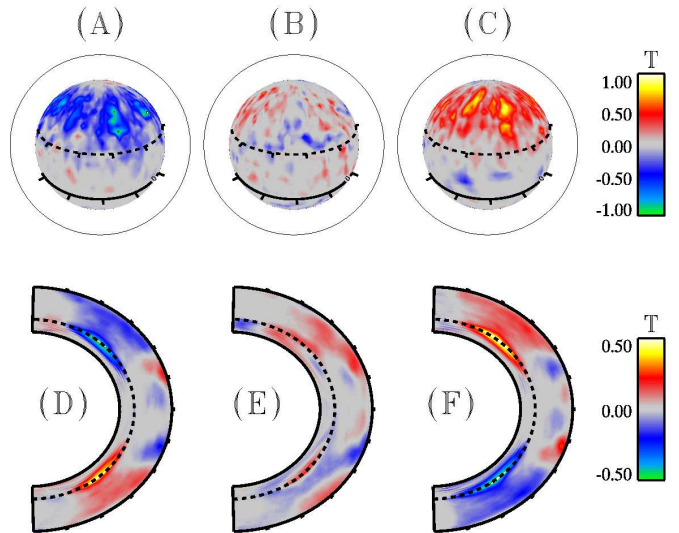


FIG. 3.— Toroidal magnetic field evolution over the course of a half cycle. The upper row shows projections of the toroidal component at the core-envelope interface in the northern hemisphere, with the thick solid and dashed lines denoting the equator and the  $30^\circ$  latitude circle, respectively. Panels (A) and (C) correspond to cycle maxima, and panel (B) to a minimum. The lower row shows meridional cross-sections of the zonally averaged toroidal component  $\langle B_\phi \rangle$  at the instants corresponding to the panels of the upper row. A dashed line marks the location of the core-envelope interface.

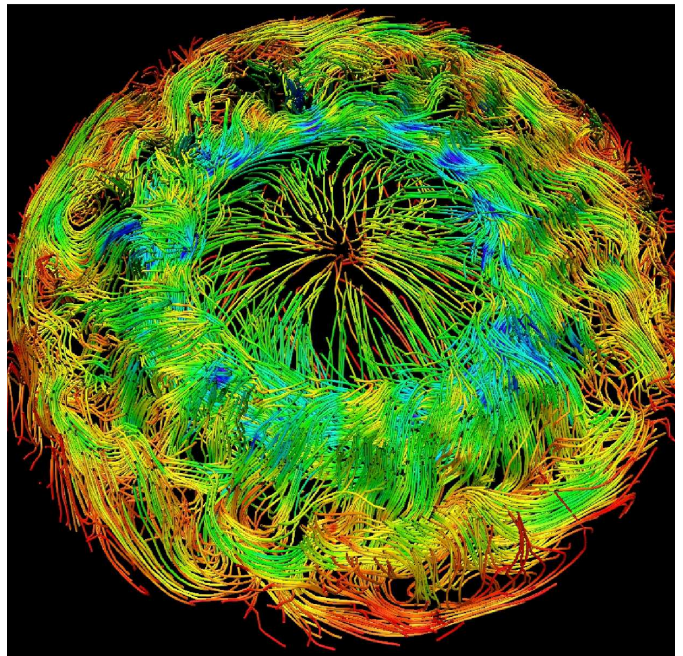


FIG. 4.— Magnetic field line tracings inside the region located above the  $30^\circ$  latitude circle; compare with Fig. 3.

polarity laws. Notably, the high-latitude flank of each wreath also exhibits a weak equatorward migration over the course of each cycle, although they appear at too high latitudes compared to the activity belts that are inferred from solar magnetograms. The evolution of the radial magnetic field component at the surface is characterized by a strong dipole moment well aligned with the

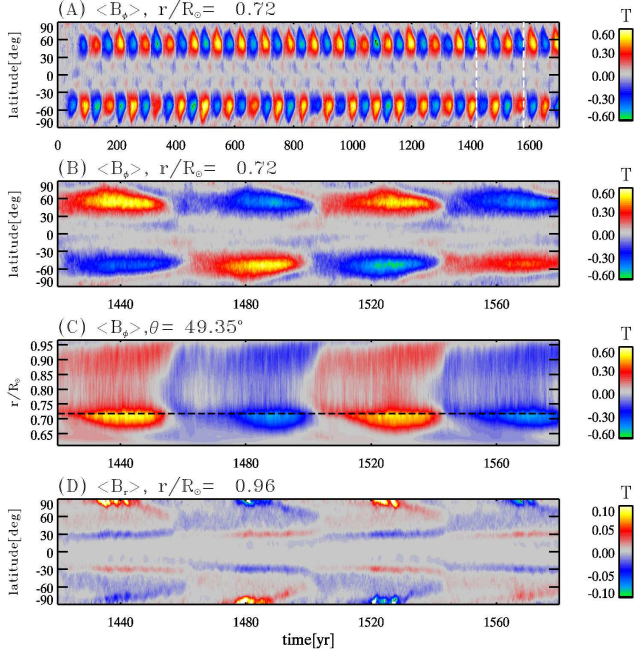


FIG. 5.— Evolution of the zonally averaged toroidal magnetic field component  $\langle B_\phi \rangle$  as a function of latitude and time at the core-envelope interface for the full temporal extent of the simulation (panel A) and for the time interval [1420, 1580]yr (panel B) — the latter is denoted by the two vertical dashed lines in panel (A). Panel (C) shows  $\langle B_\phi \rangle$  as a function of radius at high latitude and panel (D) displays the evolution of the zonally averaged radial magnetic field component  $\langle B_r \rangle$  near the surface for the same time interval.

rotation axis (panel D), the polarity of which oscillates in-phase with that of the mean toroidal field component, in contrast to the  $\pi/2$  phase lag observed on the Sun.

The generation and destruction of the large-scale cyclic magnetic field taking place in our experiment implies the conversion of kinetic energy into magnetic energy and of magnetic energy into kinetic energy via the work done by the induction and Lorentz forces (Racine et al. 2011). The Lorentz force modulates the velocity field and the heat transport by convective motions, which are sustained by the input of thermal energy into the system. In Cossette et al. (2013) the authors reported on the in-phase variation of the net enthalpy flux with total magnetic energy  $E_m \equiv (2\mu)^{-1} \int \mathbf{B}^2 dV$  of the simulation. The enthalpy flux can be written in terms of the perturbations with respect to the reference state of the anelastic approximation

$$\mathbf{F}_e \equiv \left( c_p \frac{\rho_o T_o}{\Theta_o} (\Theta - \Theta_o) + p - p_o \right) \mathbf{u} = \rho_o c_p (T - T_o) \mathbf{u}; \quad (16)$$

e.g. see Miesch (2005). The net enthalpy flux across a spherical surface  $\partial\Omega$  at a given radius is

$$\begin{aligned} L_e(r) &\equiv \int_{\partial\Omega} \left( c_p \frac{\rho_o T_o}{\Theta_o} (\Theta - \Theta_o) + (p - p_o) \right) u_r d\sigma \\ &+ \int_{\partial\Omega} \left( c_p \frac{\rho_o T_o}{\Theta_o} (\Theta_o - \bar{\Theta}) + (p_o - \bar{p}) \right) u_r d\sigma, \\ &= c_p \frac{\rho_o T_o}{\Theta_o} \int_{\partial\Omega} u_r \Delta\Theta d\sigma + \int_{\partial\Omega} u_r \Delta p d\sigma. \end{aligned} \quad (17)$$

where  $d\sigma \equiv r^2 \cos\theta d\theta d\phi$ . In (17) we have expressed the net enthalpy flux in terms of the perturbations  $\Delta\Theta \equiv \Theta - \bar{\Theta}$  and  $\Delta p = p - \bar{p}$  with respect to the simulation mean, using the fact that both the reference state and simulation mean are spherically symmetric, and that  $\int_{\partial\Omega} \rho_o u_r d\sigma = 0$  given (4) and impermeable bottom and top boundaries (cf. Appendix A). The first term on the rhs of (17) is a net internal energy flux (or heat flux) and the second is the net amount of work done by pressure forces. Inspection of Fig. 1C shows that most upflows and downflows carry, respectively, positive and negative perturbations  $\Delta\Theta$ . A smaller fraction carry perturbations of the opposite sign as a result of fluid entrainment, thereby contributing to a net positive heat flux; see Fig. 1 in Cossette et al. (2013). The pressure work term is smaller than the net heat flux by more than one order of magnitude, and therefore we focus solely on assessing the heat-flux contribution to the enthalpy flux modulation.

#### 4. MODULATED HEAT TRANSPORT

Entropy redistribution is governed by the potential temperature equation (2). Using (4), it may be written as

$$\frac{\partial\Theta'}{\partial t} = -\frac{1}{\rho_o} \nabla \cdot (\mathbf{F}_\Theta) - \alpha\Theta' + \mathcal{H}(\Theta'), \quad (18)$$

where the first term on the rhs combines the advective terms  $-\mathbf{u} \cdot \nabla\Theta'$  and  $-\mathbf{u} \cdot \nabla\Theta_a$  on the left and right-hand-sides of (2), with  $\mathbf{F}_\Theta \equiv \rho_o \mathbf{u}\Theta$ . Analyzing (2) in terms of its discrete counterpart inside the model algorithm shows that the first and second terms on the rhs of (2) constitute the dominant contributions, with  $\mathcal{H}(\Theta')$  being smaller by more than two orders of magnitude (cf. section 10.1 in Appendix C).

To understand the physical mechanism causing the convective flux modulation we examine the role of each contribution on the rhs of (18). First, we consider the total entropy rate-of-change that is associated with an infinitesimal spherical shell  $[r, r + dr]$  at a given radius  $r$ . Multiplying (18) by  $c_p \rho_o / \Theta_o$  while neglecting radiative diffusion, using the definition of potential temperature (cf. section 2) and integrating over a spherical surface gives

$$\int_{\partial\Omega} \rho_o \frac{\partial s}{\partial t} d\sigma = \int_{\partial\Omega} c_p \frac{\rho_o}{\Theta_o} \frac{\partial\Theta'}{\partial t} d\sigma = \mathcal{S}_\Theta(r) + \mathcal{S}_\alpha(r), \quad (19)$$

where  $s$  denotes specific entropy,  $\mathcal{S}_\Theta \equiv \mathcal{S}_\Theta^u + \mathcal{S}_\Theta^d$ ,  $\mathcal{S}_\alpha \equiv \mathcal{S}_\alpha^u + \mathcal{S}_\alpha^d$ , and

$$\mathcal{S}_\Theta^u(r) \equiv -\frac{c_p}{\Theta_o} \int_{\partial\Omega(u)} \nabla \cdot \mathbf{F}_\Theta d\sigma, \quad (20)$$

$$\mathcal{S}_\Theta^d(r) \equiv -\frac{c_p}{\Theta_o} \int_{\partial\Omega(d)} \nabla \cdot \mathbf{F}_\Theta d\sigma, \quad (21)$$

$$\mathcal{S}_\alpha^u(r) \equiv -\alpha \frac{c_p}{\Theta_o} \int_{\partial\Omega(u)} \rho_o \Theta' d\sigma, \quad (22)$$

$$\mathcal{S}_\alpha^d(r) \equiv -\alpha \frac{c_p}{\Theta_o} \int_{\partial\Omega(d)} \rho_o \Theta' d\sigma. \quad (23)$$

where  $\int_{\partial\Omega(u)}$  and  $\int_{\partial\Omega(d)}$  denote, respectively, integrals over portions of a spherical surface where  $u_r \geq 0$  and

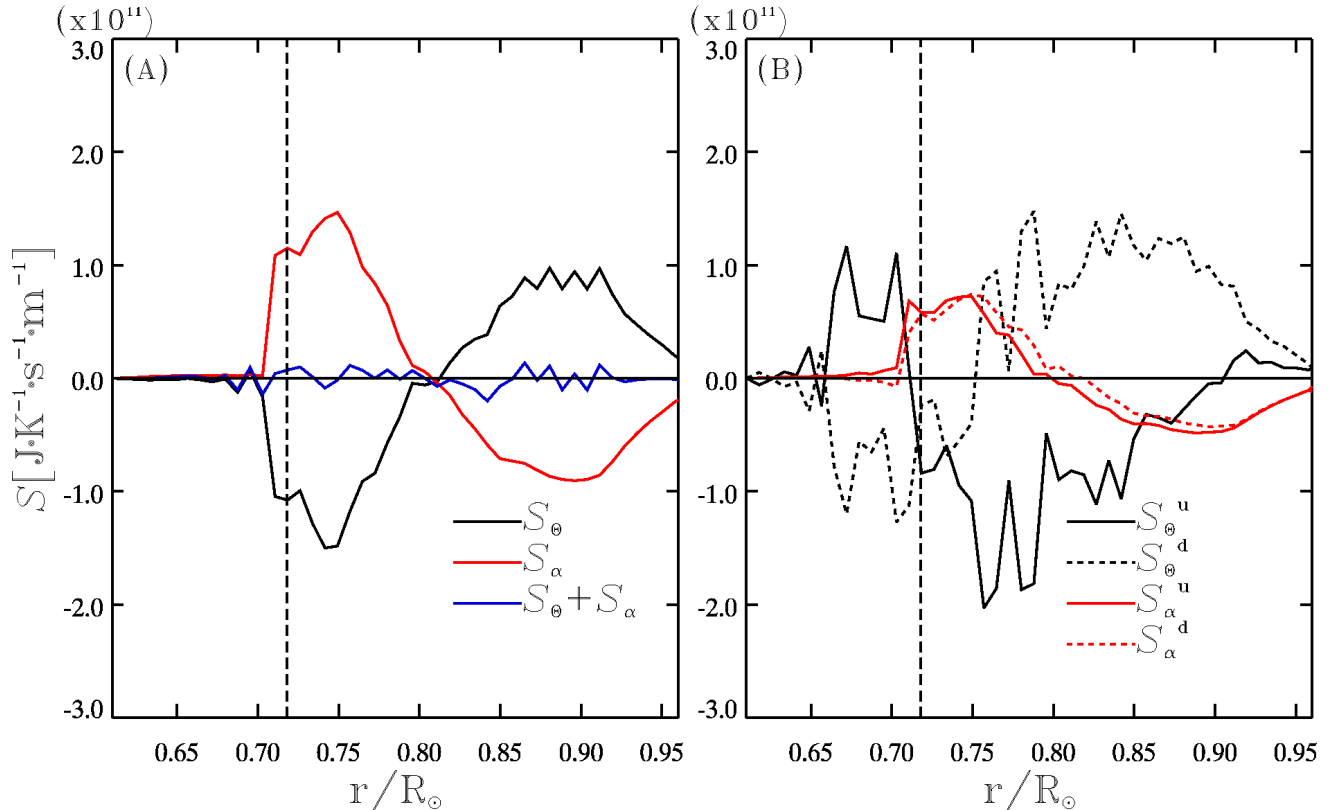


FIG. 6.— Radial profiles of contributions appearing on the rhs of (19) at an instant in time (left) and profiles of the same contributions separated for upflows and downflows (right), as described by (20)-(23).

$u_r < 0$ . The  $S_\Theta$  term is negative near the base of the convectively unstable layer and positive near its top, whereas the opposite is true of  $S_\alpha$  — see Fig. 6. The former therefore decreases the superadiabaticity of the mean potential temperature profile (cf. Fig. 1), whereas the latter does the exact opposite by increasing it. Thus, convective motions tend to homogenize the entropy field by bringing it closer to an isentropic state, whereas the Newtonian cooling opposes this effect by relaxing the entropy of fluid parcels toward the superadiabatic ambient state. Contributions from both processes nearly cancel each other out to produce a quasi-stationary state

$$S_\Theta(r) + S_\alpha(r) \approx 0. \quad (24)$$

An interesting parallel may be drawn between (10) and (24), since they reflect the thermodynamic equilibria achieved inside the Sun and in the numerical experiment, respectively. Here, Newtonian cooling (represented by  $S_\alpha$ ) balances the action of the mean resolved heat transfer (represented by  $S_\Theta$ ), thus taking the role of  $-\mathcal{H}^* = \mathcal{H}(\Theta^*)$ , which is positive near the base of the convection zone and negative near the top as a result of radiative heating and cooling. The negative  $S_\Theta$  near the base of the convection zone therefore represents the transfer of the energy deposited by radiative heating into convective motions, while the positive  $S_\Theta$  near the top represents the deposition of the energy carried by the fluid, which is then radiated into space.

Furthermore, to gain insight into the role of upflows and downflows in transporting the heat of the fluid we examine the  $\mathbf{F}_\Theta$  divergence on the rhs of (18) in terms of

their contributions. Using (4), we show in Appendix D that

$$\int_{\partial\Omega} \nabla \cdot (\rho_o \mathbf{u} \Theta) d\sigma = \int_{\partial\Omega} \rho_o u_r \frac{\partial \Theta'}{\partial r} d\sigma + \int_{\partial\Omega} \Theta' \frac{\partial \rho_o u_r}{\partial r} d\sigma. \quad (25)$$

The first and second terms on the rhs of (25) correspond, respectively, to the advection of the entropy perturbations in the radial direction and to local entropy accumulation/depletion due to a change of radial momentum with depth. The former is expected to dominate in the bulk of the unstable layer where the convective velocities are large; whereas the latter should become important near the boundaries where  $u_r$  must vanish. In particular, since  $\partial \Theta' / \partial r > 0$  inside the bulk of the convection zone (cf. Fig. 1C), the integral in the first term will receive a positive contribution from regions where  $u_r > 0$  (i.e.  $S_\Theta^u < 0$ ) and a negative one from regions where  $u_r < 0$  (i.e.  $S_\Theta^d > 0$ ). This picture is consistent with Fig. 6, which shows that  $S_\Theta^u < 0$  and  $S_\Theta^d > 0$  within the bulk of the convection zone.

Further insight into the nature of the heat transport may be gained by considering the integrals of each forcing over a portion of the convection zone. Defining  $T_r \equiv \int_{\Omega_r} T_o \rho_o dV / \int_{\Omega_r} \rho_o dV$  to be the average reference state temperature associated with a spherical shell  $\Omega_r$  extending from the base of the domain ( $r = r_b$ ) up to an arbitrary radius  $r$ , using the second law of thermodynamics and integrating (19) from  $r_b$  to  $r$  yields an expression for the total internal energy rate-of-change corresponding

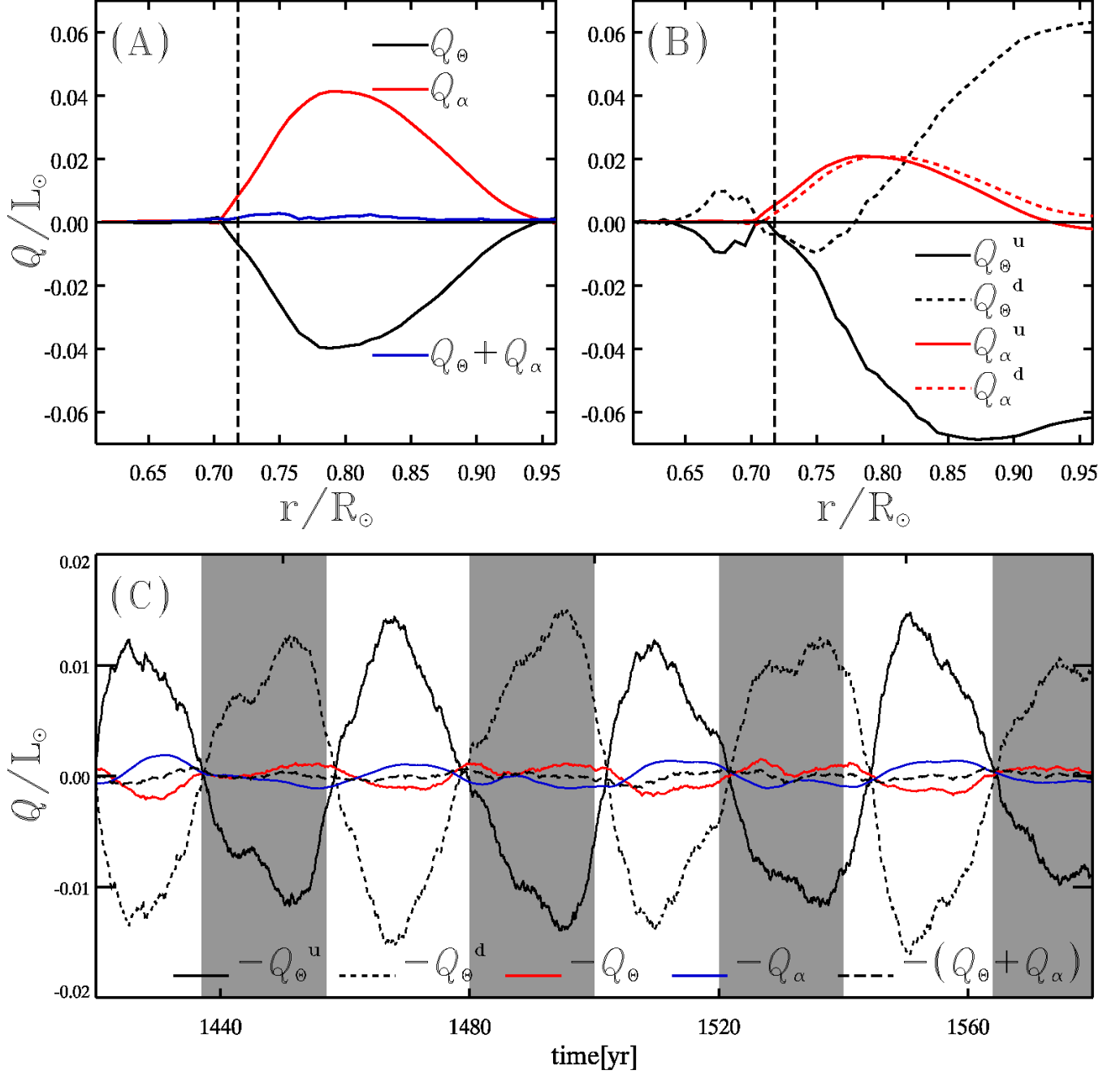


FIG. 7.— Instantaneous radial profiles of contributions to the rhs of (26) — panels (A) & (B), and their evolution with time (C). Shaded areas correspond to 20yr intervals centered about total magnetic energy maxima. In panel (C), the temporal mean of each quantity has been subtracted for clarity.

to that shell

$$\frac{\partial Q_r}{\partial t} = T_r \frac{\partial S_r}{\partial t} = Q_\Theta(r) + Q_\alpha(r), \quad (26)$$

where  $Q_\Theta \equiv Q_\Theta^u + Q_\Theta^d$ ,  $Q_\alpha \equiv Q_\alpha^u + Q_\alpha^d$ , and

$$Q_\Theta^u(r) \equiv T_r \int_{r_b}^r S_\Theta^u dr \quad (27)$$

$$Q_\Theta^d(r) \equiv T_r \int_{r_b}^r S_\Theta^d dr \quad (28)$$

$$Q_\alpha^u(r) \equiv T_r \int_{r_b}^r S_\alpha^u dr, \quad (29)$$

$$Q_\alpha^d(r) \equiv T_r \int_{r_b}^r S_\alpha^d dr. \quad (30)$$

$r/R_\odot$	Mean( $-Q_\Theta$ )	$\sigma(-Q_\Theta)$	Corr( $-Q_\Theta, E_m$ )
0.92	0.0063	0.0009	0.6681
0.90	0.0114	0.0009	0.6879
0.88	0.0203	0.0009	0.7138
0.86	0.0287	0.0010	0.7324
0.84	0.0341	0.0010	0.7425
0.82	0.0397	0.0010	0.7501
0.80	0.0411	0.0010	0.7423
0.79	0.0414	0.0010	0.7461
0.76	0.0361	0.0010	0.7436
0.75	0.0284	0.0010	0.7344
0.73	0.0180	0.0011	0.7078
0.72	0.0089	0.0011	0.6690

TABLE 1

STATISTICAL PROPERTIES OF THE CONVECTIVE HEAT LUMINOSITY MODULATION AT VARIOUS DEPTHS. SECOND AND THIRD COLUMNS SHOW, RESPECTIVELY, THE TEMPORAL MEAN AND STANDARD DEVIATION OF  $-Q_\Theta$ , WHILE THE FOURTH COLUMN DISPLAYS THE LINEAR CORRELATION COEFFICIENT COMPUTED FOR THE 5-YEAR RUNNING AVERAGES OF  $-Q_\Theta$  AND THE TOTAL MAGNETIC ENERGY TIMESERIES  $E_m$ .

The sum  $Q_\Theta \equiv Q_\Theta^u + Q_\Theta^d$  is everywhere negative inside the unstable layer (Fig. 7A) and therefore corresponds to an energy sink. By contrast, the Newtonian-cooling contribution  $Q_\alpha \equiv Q_\alpha^u + Q_\alpha^d$  acts everywhere as a source ( $Q_\alpha > 0$ ) and nearly cancels out  $Q_\Theta$  to produce a quasi-stationary state  $\partial Q_r / \partial t \approx 0$  (red curve). Moreover, since  $u_r(r_b, \theta, \phi) = 0$  at the lower boundary, we have

$$\begin{aligned}
Q_\Theta &= -\frac{c_p T_r}{\Theta_o} \int_{r_b}^r \int_{\partial\Omega} \nabla \cdot \mathbf{F}_\Theta dV \\
&= -\frac{c_p T_r}{\Theta_o} \left( \int_{\partial\Omega} (\rho_o(r) u_r(r, \theta, \phi) \Theta'(r, \theta, \phi) \right. \\
&\quad \left. - \rho_o(r_b) u_r(r_b, \theta, \phi) \Theta'(r_b, \theta, \phi)) d\sigma \right. \\
&= -\frac{c_p \rho_o(r) T_r}{\Theta_o} \int_{\partial\Omega} u_r(r, \theta, \phi) \Theta'(r, \theta, \phi) d\sigma, \quad (31)
\end{aligned}$$

whereby  $-Q_\Theta$  has the interpretation of a net convective heat flux. The latter is everywhere positive inside the unstable layer, remains positive over a short distance below the interface with the stable layer, and subsequently changes sign (Fig. 7). The persistence of the convective heat flux below the convection zone and into the stably stratified interior and its subsequent change of sign is a consequence of penetrative convection, and is also present in other simulations of solar convection (e.g. Miesch et al. (2000); Pal et al. (2007)).

The signature of the magnetic cycle is present in both  $Q_\Theta$  and  $Q_\alpha$  (Fig. 7, panel C), which are anti-correlated and correlated with the total magnetic energy, respectively. Most importantly, the out-of-phase modulation of  $Q_\Theta$  corresponds to an in-phase variation of the net convective heat flux ( $-Q_\Theta$ ) with total magnetic energy (red curve in panel C), which results from corresponding modulations of upflow and downflow contributions  $-Q_\Theta^u$  and  $-Q_\Theta^d$ . Table 1 shows that the standard deviation of the  $-Q_\Theta$  modulation reaches a significant fraction of its temporal average, and that it correlates very well with the total magnetic energy at every depth in the unstable layer. Interestingly, the standard deviation is largest near the core-envelope interface where the large-scale toroidal

magnetic field wreaths are located (cf. Fig. 5).

The imbalance between upflow and downflow contributions  $Q_\Theta^d$  and  $Q_\Theta^u$  is therefore responsible for producing an enhanced net convective heat flux at cycle maximum, and must result from modulating upflows and downflows differently. According to (25), this implies an upflow/downflow modulation that is asymmetric with respect to their associated (i) convective velocity amplitudes, (ii) vertical momentum gradient, (iii) entropy perturbation amplitudes and/or (iv) entropy gradient.

## 5. DYNAMICAL DRIVERS OF THE FLOW MODULATION

Ultimately, the heat transport modulation documented in the previous section must take place as a result of the Lorentz force's action on the flow field. Which aspect of the Lorentz force leads to an asymmetric upflow/downflow modulation must therefore be determined through careful inspection of the balance of forces on the rhs of (1) and the flow response that they induce. The equation governing the evolution of radial momentum can be written as

$$\frac{\partial \rho_o u_r}{\partial t} = F_a + F_\varphi + F_g + F_c + F_t \quad (32)$$

where  $F_a$ ,  $F_\varphi$ ,  $F_g$ ,  $F_c$  and  $F_t$  correspond, respectively, to minus the radial momentum flux divergence, minus the pressure gradient's radial component, the buoyancy force, Coriolis force and magnetic tension; see Appendix C for the definition of each term on the rhs of (32). To develop an intuition for the nature of each forcing term  $F_X$ , we compute their mean value inside a given radial velocity and temperature deviation range  $\mathcal{I} \equiv [u_r, u_r + \delta u_r] \times [\Delta T', \Delta T' + \delta(\Delta T')]$  on a spherical surface at a given depth, namely

$$\delta F_X(u_r, \Delta T', r) \equiv \frac{1}{N_{\mathcal{I}}} \sum_{\mathbf{i} \in \mathcal{I}} F_X(\phi, \theta, r)_{\mathbf{i}}, \quad (33)$$

where  $\mathbf{i}$  denotes a grid point and  $N_{\mathcal{I}}$  is the number of grid points contained in  $\mathcal{I}$ .

Figure (8) shows each term's associated mean force distribution  $\delta F_X$  close to the bottom of the unstable layer at  $r = 0.76 R_\odot$ . Here,  $\delta F_s$  is the distribution associated with  $F_s \equiv F_\varphi + F_g + F_c$ , namely the sum of pressure gradient, buoyancy and Coriolis forces (panel A). The near cancellation of  $F_\varphi$  and  $F_g$  (not shown) leads to predominantly positive and negative  $F_s$  where  $u_r > 0$  and  $u_r < 0$ , which means that buoyancy and pressure forces act together to impart upward and downward accelerations to the upflows and downflows. Consequently, in a statistically-steady state ( $\partial u_r / \partial t \approx 0$ ) upflows and downflows are characterized by  $Du_r / Dt > 0$  ( $\delta F_a < 0$ ) and  $Du_r / Dt < 0$  ( $\delta F_a > 0$ ); see panel B. Magnetic tension is predominantly negative and positive inside upflows and downflows, respectively (panel C); it therefore opposes the work done by buoyancy and pressure forces (panel A).

To understand how each force impacts the radial momentum's rate-of-change, we compute the total force associated with a given term  $F_X$  that is acting on upflows and downflows inside the infinitesimal spherical shell  $[r, r + dr]$  at depth  $r$

$$\mathcal{F}_X^u(r) \equiv dr \int_{\partial\Omega(u)} F_X d\sigma,$$

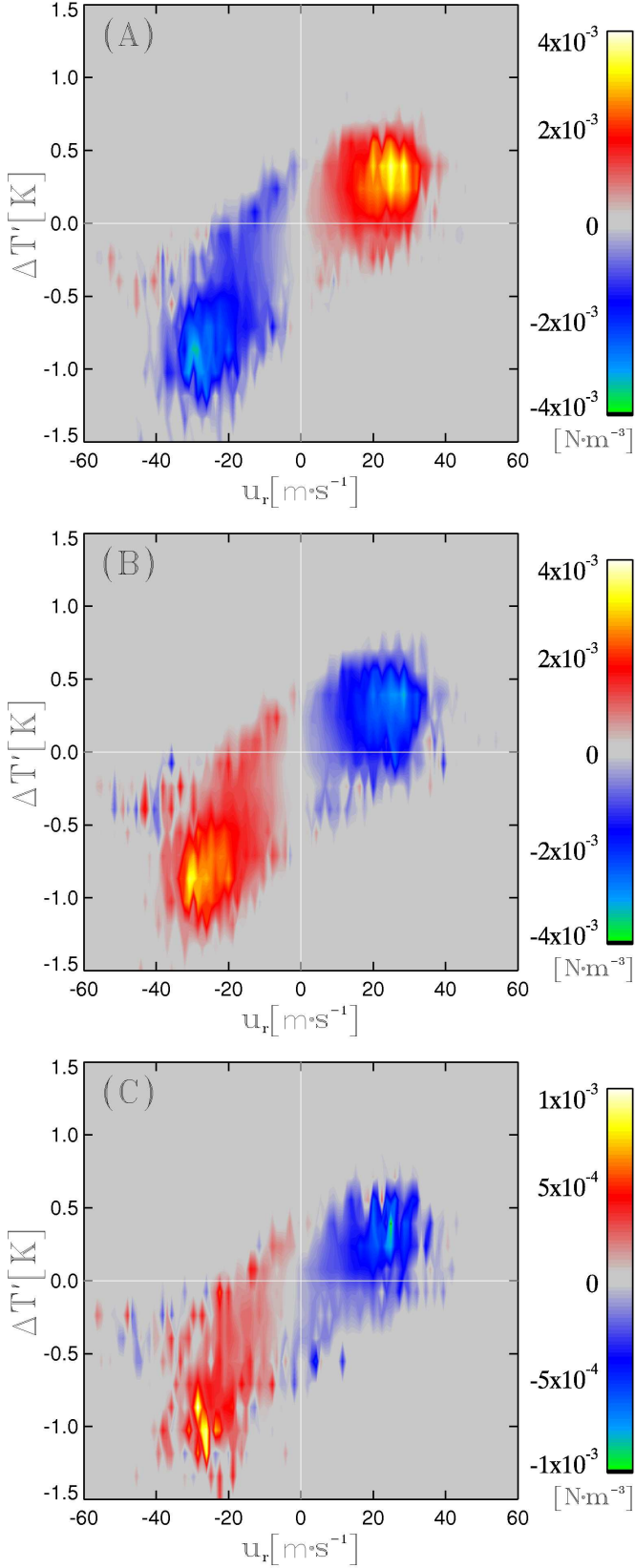


FIG. 8.— Mean force density distributions averaged 1.7 yr about an instant taken half-way through the rising phase of a magnetic cycle at  $r/R_{\odot} = 0.76$ . Panels (A), (B) and (C) show, respectively,  $\delta F_s$ ,  $\delta F_a$  and  $\delta F_t$ .

$$\mathcal{F}_X^d(r) \equiv dr \int_{\partial\Omega(d)} F_X d\sigma. \quad (34)$$

Integrating (32) over the surface of a given shell therefore yields

$$\frac{\partial \mathcal{V}}{\partial t} = \frac{\partial \mathcal{V}^u}{\partial t} + \frac{\partial \mathcal{V}^d}{\partial t}, \quad (35)$$

where  $\mathcal{V}^u = \mathcal{V}^u(r) \equiv dr \int_{\partial\Omega(u)} \rho_o u_r d\sigma$  and  $\mathcal{V}^d = \mathcal{V}^d(r) \equiv dr \int_{\partial\Omega(d)} \rho_o u_r d\sigma$ , with  $\mathcal{V} \equiv \mathcal{V}^u + \mathcal{V}^d$ . Consequently, we have the following equations governing the evolution of total upflow and downflow momentum

$$\frac{\partial \mathcal{V}^u}{\partial t} = \mathcal{F}_a^u + \mathcal{F}_s^u + \mathcal{F}_t^u, \quad (36)$$

$$\frac{\partial \mathcal{V}^d}{\partial t} = \mathcal{F}_a^d + \mathcal{F}_s^d + \mathcal{F}_t^d. \quad (37)$$

Most importantly, the anelastic mass continuity equation (4) requires that  $\mathcal{V}(r) = 0$  for every depth (cf. Appendix A), whereby  $\partial \mathcal{V} / \partial t = 0$  and

$$\partial \mathcal{V}^u / \partial t = -\partial \mathcal{V}^d / \partial t \quad (38)$$

at every depth.

Radial profiles of each force (Fig. 9A) show that the total magnetic tension that is exerted on the upflows is everywhere negative ( $\mathcal{F}_t^u < 0$ ) inside the convection zone, whereas it is everywhere positive inside downflows ( $\mathcal{F}_t^d > 0$ ) except near the top of the domain ( $r > 0.85R_{\odot}$ ). Likewise, we have  $\mathcal{F}_s^u > 0$  and  $\mathcal{F}_s^d < 0$  inside the bulk of the unstable layer. The net force  $\mathcal{F}_s^u + \mathcal{F}_t^u > 0$  acting on upflows produces a net radial momentum loss through each shell ( $\mathcal{F}_a^u < 0$ ). Similarly for downflows, we have  $\mathcal{F}_s^d + \mathcal{F}_t^d < 0$  and  $\mathcal{F}_a^d > 0$ . This produces an upflow momentum rate-of-change  $\partial \mathcal{V}^u / \partial t < 0$ , which is equal and opposite to the net momentum rate-of-change associated with downflows  $\partial \mathcal{V}^d / \partial t > 0$  at every depth, as per the mass continuity constraint (38).

Each term  $\mathcal{F}_X$  is strongly modulated by the magnetic cycle near the base of the convection zone where the large-scale field is concentrated (Fig. 9B). One very striking feature is the asymmetry characterizing the evolutions of the total magnetic tensions  $\mathcal{F}_t^u$  and  $\mathcal{F}_t^d$  inside upflows and downflows. In particular, the amplitude of the  $\mathcal{F}_t$  modulation is larger in upflows than in downflows. To satisfy (38), the system responds to the increased magnetic tension in upflows with a simultaneous increase of both  $\mathcal{F}_s^u$  and  $\mathcal{F}_s^d$ 's magnitudes.

The  $\mathcal{F}_s$  term is the sum of buoyancy  $\mathcal{F}_g$ , Coriolis  $\mathcal{F}_c$ , and pressure gradient  $\mathcal{F}_\varphi$ , which develop their own responses to the increased magnetic tension at cycle maximum (Fig. 9C). While the forces acting on upflows and downflows maintain similar amplitudes, this is not the case for the buoyancy force, which appears to be more strongly modulated inside the downflows compared to upflows. This is substantiated by probability density functions (PDFs) of the radial velocity  $u_r$  and deviations  $\Delta\Theta \equiv \Theta - \bar{\Theta}$  with respect to the mean potential temperature (Fig. 10). Comparing the potential temperature perturbations PDFs at cycle minimum and maximum at  $r = 0.76R_{\odot}$  (panel D) shows that the change in the perturbations' magnitude at cycle maximum with respect

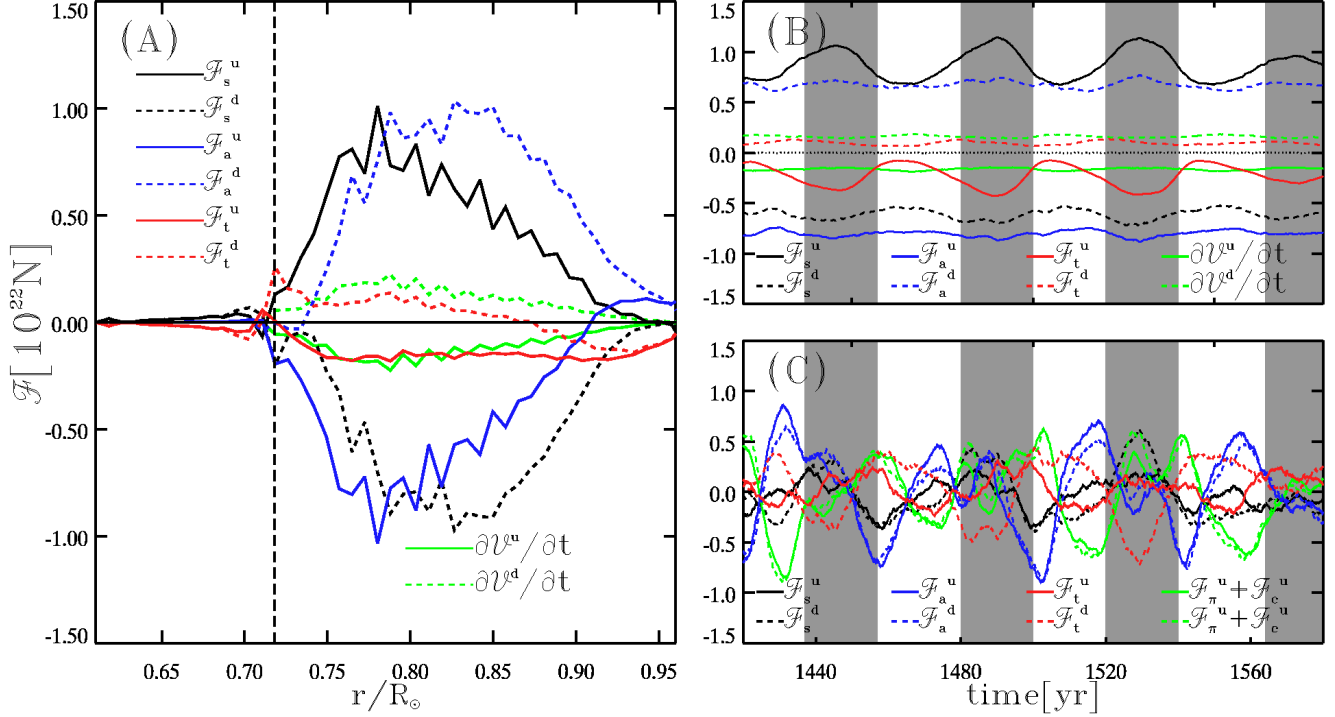


FIG. 9.— Radial profiles of total forces that are exerted on upflows (solid lines) and downflows (dashed lines) at an instant taken half-way through the rising phase of a magnetic cycle (panel A). Timeseries (5 yr running averages) of total forces exerted on upflows and downflows at  $r = 0.76R_{\odot}$  (panels B and C).

to cycle minimum is greater in downflows than in upflows, which is consistent with the larger buoyancy force modulation inside downflows observed in Fig. 9B.

Consequently, the upflow/downflow asymmetry characterizing the evolutions of magnetic tensions  $\mathcal{F}_t^u$  and  $\mathcal{F}_t^d$  induces corresponding asymmetries in the evolution of buoyancy forces  $\mathcal{F}_g^u$  and  $\mathcal{F}_g^d$  as part of the flow's response to fulfill the mass continuity constraint. These buoyancy forces develop through the modulation of  $\Theta^u$  and  $\Theta^d$ , which determine the character of the enthalpy flux and convective heat flux (cf. Fig. 7). This suggests that the imbalance between upflow and downflow contributions to heat transport  $\mathcal{Q}^u$  and  $\mathcal{Q}^d$  and the resulting net convective heat flux modulation result from the magnetic tension imbalance inside upflows and downflows that takes place as the level of magnetism changes with the cycle.

## 6. IMPACT ON IRRADIANCE VARIATIONS

The heat transported by convection is redistributed inside the domain by the Newtonian cooling (Fig. 7) so that the total heat flux at the top boundary is zero. However, we may assess the temperature and heat flux modulations induced by cyclic activity at the surface if we assume that the propagation of thermodynamic perturbations generated inside the interior is well approximated by turbulent diffusion (Spruit 1977; Stix 1981). The problem amounts to solving the steady-state heat diffusion equation

$$\nabla \cdot (\delta \mathbf{F}) = 0, \quad (39)$$

where  $\delta \mathbf{F}(n, x, y, z) \equiv K \nabla \delta T$  is a normalized flux disturbance associated with a temperature perturbation

$\delta T(n, x, y, z)$  of the form  $\approx f(n, z) \exp(ik_x x + ik_y y)$ , and  $K = K_o(z+z_1)^2$  is a depth-dependent turbulent diffusion coefficient, with  $K_o = 2.94 \times 10^{-9} \text{m}^{-1} \cdot \text{K}^{-1}$  and  $z_1 = 127$  km a reference depth. Here,  $n \equiv \pi R_{\odot} (k_x^2 + k_y^2)^{1/2} / 2$  corresponds to the number of waves on half a solar circumference. Solving (39) subject to the radiative (Stefan-Boltzmann) boundary condition  $\delta F \equiv 4\delta T/T_s$  at  $z = 0$  ( $T_s = 6540\text{K}$ ) yields analytical expressions for  $\delta T$  and  $\delta F$ , from which amplitude response functions for temperature and heat flux disturbances induced at the surface may be derived

$$\begin{aligned} R_T(n, z) &\equiv f(n, 0)/f(n, z), \\ R_F(n, z) &\equiv K(0)f'(n, 0)/K(z)f'(n, z), \end{aligned} \quad (40)$$

where  $f'(n, z) \equiv df/dz$ ; see equations (3) and (4) from Stix (1981). Perturbations with higher harmonics decay faster, as expected (Fig. 11).

The azimuthally-averaged temperature perturbations are all characterized by strong latitudinal dependencies ( $n \sim 1 - 2$ ) having typical amplitudes  $\sim 0.10\text{K}$ . According to Fig. 11, perturbations with  $n \sim 1 - 2$  everywhere in the convection zone are attenuated by a factor  $\sim 1/4$  once they reach the surface. The associated change in the heat flux given by the radiative boundary condition is  $\delta F \sim 4\delta T/T_s = 1.7 \times 10^{-5}$ , which is approximately 100 times smaller than the observed 0.1% decadal change in TSI. By comparison, perturbations to the heat flux are attenuated by orders of magnitude more than the associated temperature disturbances (Fig. 11). Fig. 2 of Cossette et al. (2013) shows the cyclic variation of the longitudinally averaged enthalpy flux as a function of latitude at  $r = 0.87R_{\odot}$ . The flux variation is characterized by a  $n = 2$  oscillation in latitude

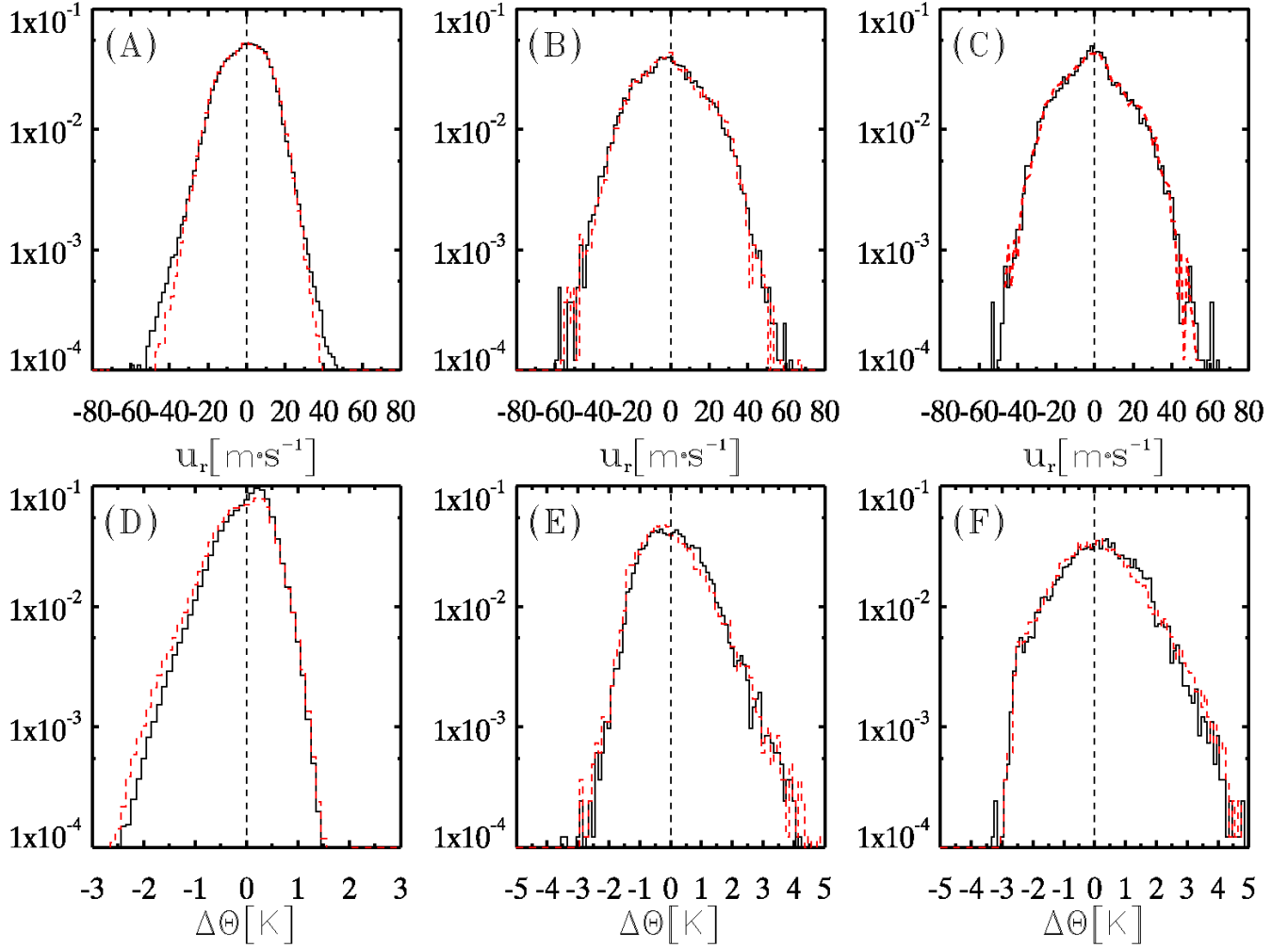


FIG. 10.— PDFs of radial velocity amplitudes (top row) and potential temperature perturbations (bottom) averaged over all minima (black curves) and maxima (red curves) at  $r = 0.76R_{\odot}$  (right),  $r = 0.82R_{\odot}$  (center), and  $r = 0.88R_{\odot}$  (left).

with typical amplitude  $\sim 10^6 \text{ W} \cdot \text{m}^{-2}$  from cycle minima to maxima in each hemisphere. Therefore, according to Fig. 11 the flux perturbation is damped by a factor  $\sim 100$ , which gives a flux variation at the surface  $\delta F \sim 10^4 \text{ W} \cdot \text{m}^{-2} / (L_{\odot} / 4\pi R_{\odot}^2) \sim 10^{-4}$ .

## 7. DISCUSSION

We have investigated the physical mechanism responsible for the convective heat flux modulation produced in a global MHD simulation of solar convection. The initial random magnetic field that is specified in the simulation develops into a well-organized large scale magnetic component undergoing hemispheric polarity reversals at a 40 yr cadence. The interaction of the cycling magnetic field with the flow produces an in-phase variation of the convective heat flux with the total magnetic energy of the simulation.

We find that this variation is related to differences in the way upflow and downflow contributions to heat transport are modulated by the cycle. This so-called upflow/downflow asymmetry can be traced back to corresponding asymmetries in the magnetic tension forces acting on upflows and downflows. Magnetic tension works against buoyancy and pressure gradient forces to

suppress flow motion. In particular, upflows are more strongly modulated by the magnetic tension compared to downflows. To satisfy the mass continuity constraint, the flow responds to the increased magnetic tension with a change in the pressure gradient and buoyancy force. The consequent modulation of the entropy perturbations is what leads to the upflow/downflow asymmetry and the in-phase variation of the convective heat flux with total magnetic energy.

A modulation of convective heat transport by the large-scale magnetic cycle has also been observed in a cycling convective dynamo solution produced using the ASH code (Augustson et al. 2015). The enthalpy flux in this simulation decreases at cycle maximum, whereas we find the opposite behavior in ours. The origin of the discrepancy with the ASH result could be related to differences in the thermodynamic constraints that are imposed in each simulation. The model of Augustson et al. (2015) drives convection by maintaining a constant solar luminosity via the specification of flux-transmitting conditions at the upper and lower boundaries, whereas our model maintains a convectively unstable stratification over a time scale long compared to the cycle's period by relaxing the entropy of fluid parcels to that of the

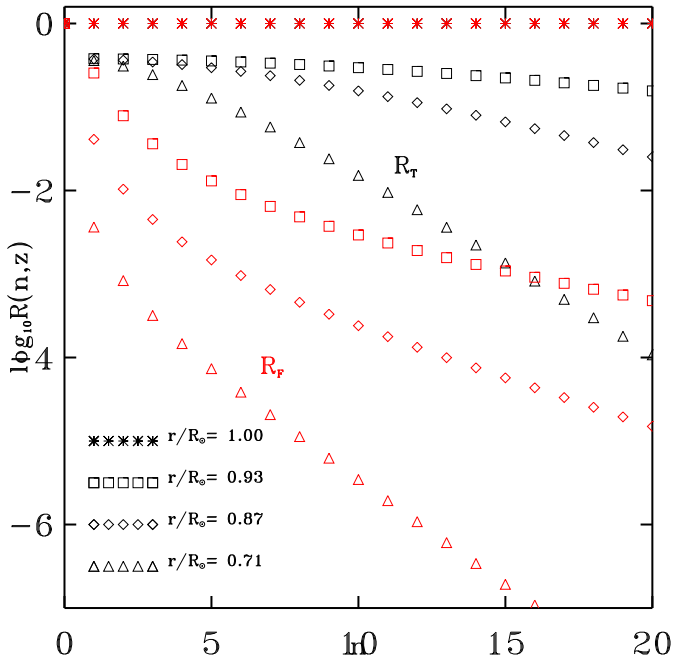


FIG. 11.— Temperature and heat flux amplitude response functions  $R_T(n, z)$  and  $R_F(n, z)$  corresponding to various depths  $z$ .

superadiabatic ambient state  $\Theta_a$ . Thus, in the ASH simulation the external energy reservoir is accessed via the boundary fluxes, whereas in our simulation it is accessed locally via the Newtonian cooling term.

It is important to note that global MHD experiments of solar convection are currently unable to resolve the small-scale flows present in the subphotospheric layers, which account for the transport of energy between the deep convection zone and the photosphere where the energy generated in the core is released by photons. In global simulations that rely on heating and cooling terms at the upper and lower boundaries to drive convection, the transport of energy near the top boundary is often modeled via a flux proportional to the entropy gradient (e.g. Miesch et al. (2008); Augustson et al. (2015); Featherstone & Hindman (2016)). The simulation presented in this paper does not rely on heating or cooling at the boundaries, but instead drives convection internally by maintaining a mean superadiabatic stratification throughout the domain. Because solutions are sought in terms of fluctuations about a superadiabatic  $\Theta_a$  profile in the convection zone, the solution's dependence on dissipation/diffusion is greatly reduced. This enables dynamic equilibria that might have been unreachable on dissipative paths of integrations starting with  $\Theta_a \equiv \Theta_0$  and a large amplitude heating/cooling forcing applied at the model lower/upper boundaries.

Determining the potential effect that the cycling large-scale magnetic field has on the heat transport and the irradiance output at the Sun's surface is important for assessing the impact of solar variability on the Earth's climate. Using a model based on the approximation of turbulence as diffusion, we estimated that the change in the irradiance at the surface in response to thermodynamic perturbations generated by the magnetic cycle is on the order of 0.01% or smaller. As expected, the strong

attenuation of temperature and heat flux disturbances by turbulent diffusion effectively screens the deep-seated flux modulation from the surface (Stix 1981). This result seems to be consistent with the very small amplitudes of the variations of the photospheric temperature and solar radius that have been inferred from observations so far (c.f. section 1). Such small variations are likely to be insignificant for climate change on decadal or even multi-decadal time scales (Foukal et al. 2006).

Alternately, it may be that the approximation of convection by turbulent diffusion is fundamentally inadequate to represent the highly non-local heat transport in stellar interiors, where upflows and downflows tend to remain coherent over several pressure scale heights (e.g. Rieutord & Zahn (1995); Spruit (1997); Nordlund et al. (2009)). In this case, the relevant time scale for the change in the irradiance induced by a deep-seated modulation of the large-scale magnetic field is the plumes' transit time across the convecting layer (Cossette & Rast 2016). Higher resolution global simulations and observations that are able to capture such non-local effects while coupling the deep convection zone to the radiative boundary layer of the star may be required to assess their contribution to the variations of the irradiance in the presence of a large-scale cyclic magnetic field.

#### ACKNOWLEDGMENTS

We thank an anonymous referee for comments that helped improve the paper. The numerical experiments reported in this paper were carried out on the computing facilities of Calcul Québec, a member of Compute Canada consortium. J.-F.C. acknowledges the support of the University of Colorado's George Ellery Hale Postdoctoral Fellowship. P.C. acknowledges support by Canada Foundation for Innovation (Grant No. 18382), Canada Research Chair program (Grant CRC-203812) and NSERC Discovery Grant (Grant No. RGPIN/261430-2013). P.K.S. acknowledges support by funding received from the European Research Council under the European Union's Seventh Framework Programme (FP7/2012/ERC Grant agreement No. 320375). M.P.R.'s work was partially supported by NASA award NNX12AB35G.

#### 8. APPENDIX A: PERTURBATIONAL FORM OF THE GOVERNING EQUATIONS

To minimize mathematical complexity and focus on physics, the governing equations are written in Cartesian framework  $(x, y, r)$ , thus bypassing (temporarily) metric factors of the spherical domain. While the spherical form of the governing equations is discussed in the body of the paper, here we only assume periodic boundary conditions in  $x$  and  $y$ , to mimic one key aspect of the global solar case. Defining  $\Phi \equiv \{\mathbf{u}, \Theta, \varphi, \mathbf{B}\}$ , and the space and time averaged state

$$\Phi^* \equiv \overline{\Phi} \equiv \frac{1}{t^*XY} \int_{-t^*/2}^{t^*/2} \int_0^X \int_0^Y \Phi dx dy dt, \quad (41)$$

such that a stationary state  $\partial\Phi^*/\partial t \approx 0$  can be assumed, yields the following decomposition of each variable into a mean and a perturbation  $\tilde{\Phi} \equiv \{\tilde{\mathbf{u}}, \tilde{\Theta}, \tilde{\varphi}, \tilde{\mathbf{B}}\} \equiv \Phi - \Phi^*$ .

##### 8.1. Entropy equation

To derive the perturbation form of the entropy equation (2), consider first its generic form in the anelastic approximation (9). The equation (9) can be obtained from the generic thermodynamic principle  $T ds/dt = S_Q$  — relating the evolution of specific entropy to the heat source  $S_Q$  (per unit of mass) due to radiation diffusion and heat diffusion — using the definition of the potential temperature  $ds = c_p d \ln \Theta$  together with the Lipps & Hemler (1982) anelastic approximation  $T' \equiv \Theta' T_o / \Theta_o$ . Combining (9) with the anelastic mass continuity equation (4) leads to the conservative form

$$\begin{aligned} & \frac{\partial \rho_o \Theta}{\partial t} + \nabla \cdot (\rho_o \mathbf{u} \Theta) \\ &= \frac{\Theta_o}{T_o} \left[ \nabla \cdot \left( \kappa_r \rho_o \nabla \Theta \frac{T_o}{\Theta_o} \right) + \nabla \cdot \left( \kappa \frac{\rho_o T_o}{\Theta_o} \nabla \Theta \right) \right]. \end{aligned} \quad (42)$$

Substituting  $\Theta = \Theta^* + \tilde{\Theta}$  and  $\mathbf{u} = \mathbf{u}^* + \tilde{\mathbf{u}}$  into (42) and applying the horizontal-time average to (42) gives

$$\begin{aligned} & \frac{d}{dr} \rho_o u_r^* \Theta^* + \frac{d}{dr} \rho_o \overline{\tilde{u}_r \tilde{\Theta}^*} = \\ & \frac{\Theta_o}{T_o} \left[ \frac{d}{dr} \left( \kappa_r \rho_o \frac{d T_o}{dr} \Theta^* \right) + \frac{d}{dr} \left( \kappa \frac{\rho_o T_o}{\Theta_o} \frac{d \Theta^*}{dr} \right) \right]. \end{aligned} \quad (43)$$

Importantly, the first term on the lhs of (43) vanishes, because applying the same averaging procedure to the mass continuity equation (4) yields  $d/dr \rho_o \overline{u_r^*} = 0$ , thus implying  $\overline{\rho_o u_r^*}|_r - \rho_o \overline{u_r^*}|_{r_b} = 0$  (also  $\overline{\rho_o u_r^*}|_{r_t} - \rho_o \overline{u_r^*}|_{r_t} = 0$ ) and therefore  $\overline{u_r^*} = 0 \forall r$ , given mean impermeable boundaries at  $r = r_b$  or  $r = r_t$  (cf. section 2.3). In consequence,

$$\begin{aligned} 0 &= \frac{\Theta_o}{\rho_o T_o} \left[ \frac{d}{dr} \left( \kappa_r \rho_o \frac{d T_o}{dr} \Theta^* \right) + \frac{d}{dr} \left( \kappa \frac{\rho_o T_o}{\Theta_o} \frac{d \Theta^*}{dr} \right) \right] \\ & \quad - \rho_o^{-1} \frac{d}{dr} (\rho_o \overline{\tilde{u}_r \tilde{\Theta}^*}) \equiv \mathcal{H}(\Theta^*) + \mathcal{H}^*, \end{aligned} \quad (44)$$

or equivalently eq. (10) in section 2.2. Subtracting (44) from (9), while moving the convective derivative  $\mathbf{u} \cdot \nabla \Theta^*$  to the rhs, results in (11).

### 8.2. Momentum equation

Using (4)-(5) to rewrite the material derivative and Lorentz force term in (8) in conservative form we obtain

$$\begin{aligned} & \frac{\partial \rho_o \mathbf{u}}{\partial t} + \nabla \cdot (\rho_o \mathbf{u} \mathbf{u}) = -\rho_o \nabla \left( \frac{p - p_o}{\rho_o} \right) - \rho_o \mathbf{g} \frac{\Theta - \Theta_o}{\Theta_o} \\ & \quad + 2\rho_o \mathbf{u} \times \boldsymbol{\Omega} + \frac{1}{\mu} \nabla \cdot (\mathbf{B} \mathbf{B}) + \rho_o \mathcal{D}_{\mathbf{u}} \end{aligned} \quad (45)$$

where  $p$  includes magnetic and gas pressure. Substituting  $\boldsymbol{\Phi} = \boldsymbol{\Phi}^* + \tilde{\boldsymbol{\Phi}}$  into (45), and applying the horizontal time-average to (45) leads to

$$\begin{aligned} 0 &= -\rho_o \frac{d}{dr} \left( \frac{p^* - p_o}{\rho_o} \right) + \rho_o g \frac{\Theta^* - \Theta_o}{\Theta_o} - \frac{d}{dr} (\rho_o \overline{\tilde{u}_r \tilde{u}_r^*}) \\ & \quad + \frac{1}{\mu} \frac{d}{dr} (\overline{\tilde{B}_r \tilde{B}_r^*}), \end{aligned} \quad (46)$$

where we used the fact that the average of a perturbation vanishes, and that  $u_r^* = 0 \forall r$  to set  $\overline{\mathcal{D}_{\mathbf{u}}^*} \equiv 0$ . Defining

an auxiliary variable

$$\frac{\psi^*}{\rho_o} \equiv - \int_{r_b}^r \frac{1}{\rho_o} \left[ \frac{d}{dr} (\rho_o \overline{\tilde{u}_r \tilde{u}_r^*}) - \mu^{-1} \frac{d}{dr} (\overline{\tilde{B}_r \tilde{B}_r^*}) \right] dr', \quad (47)$$

allows to rewrite (46) as

$$0 = -\rho_o \frac{d}{dr} \left( \frac{p^* + \psi^* - p_o}{\rho_o} \right) + \rho_o g \frac{\Theta^* - \Theta_o}{\Theta_o}, \quad (48)$$

thus exposing a compact hydrostatic relation that accounts for Reynolds and Maxwell fluxes, respectively, due to the correlations of fluctuating radial velocity and radial magnetic components associated with the mean solar-state equilibrium. Subtracting (48) from the generic momentum equation (45) gives then

$$\begin{aligned} & \frac{\partial \rho_o \mathbf{u}}{\partial t} + \nabla \cdot (\rho_o \mathbf{u} \mathbf{u}) = \\ & \quad - \rho_o \nabla \left( \frac{p - p^* - \psi^*}{\rho_o} \right) - \rho_o \mathbf{g} \frac{\Theta - \Theta^*}{\Theta_o} \\ & \quad + 2\rho_o \mathbf{u} \times \boldsymbol{\Omega} + \frac{1}{\mu} \nabla \cdot (\mathbf{B} \mathbf{B}) + \mathcal{D}_{\mathbf{u}}, \end{aligned} \quad (49)$$

which upon dividing by  $\rho_o$  and using (4)-(5) gives the Lagrangian form (12).

### 9. APPENDIX B: PIECEWISE POLYTROPE

We construct  $\Theta_a$  using a piecewise-linear polytrope,

$$p_m = K \rho_m^{1+\frac{1}{m}}, \quad p_m = \rho_m R T_m, \quad \frac{dp_m}{dr} = -\rho_m g \quad (50)$$

where  $m = m(r)$  is a variable polytropic index and  $R = c_p - c_v$ . Each polytrope satisfies the equation

$$\frac{dT_m}{dr} = - \frac{g}{(1+m)R}, \quad (51)$$

which yields the following expressions for temperature, density and pressure when integrated from  $r$  to  $r + \Delta r$

$$T_m(r + \Delta r) = T_m(r) f(r), \quad (52)$$

$$\rho_m(r + \Delta r) = \rho_m(r) f(r)^m, \quad (53)$$

$$p_m(r + \Delta r) = p_m(r) f(r)^{m+1}, \quad (54)$$

where

$$f(r) \equiv 1 - \frac{rg(r)}{(m+1)RT_m(r)} \left( 1 - \frac{r}{r + \Delta r} \right).$$

and  $\Delta r$  is the radial grid spacing. Equations (52)-(54) are solved recursively to give the desired ambient profiles  $T_m(r)$ ,  $p_m(r)$  and  $\rho_m(r)$  for specified values  $T_a(r_b) = T_b$ ,  $\rho(r_b) = \rho_b$  and  $p(r_b) = p_b$  at  $r = r_b$ . The index  $m$  is used to enforce, respectively, convectively stable (subadiabatic) and unstable (superadiabatic) stratifications in regions corresponding to the radiative interior ( $r \leq r_i$ ) and convection zone ( $r > r_i$ ). Inside the stable layer,  $m$  decreases linearly up to  $r = r_i$

$$m(r) = m_s - (m_s - m_{ad}) \frac{r - r_b}{r_i - r_b}, \quad (55)$$

where  $m_{ad} = 1/(\gamma - 1)$ , with  $\gamma = c_p/c_v = 5/3$  the ratio of specific heats. Transitions from subadiabatic to

superadiabatic stratifications at the interface and from superadiabatic to adiabatic near the surface are modeled using a combination of hyperbolic functions

$$m(r) = m_{\text{ad}} + \frac{1}{2}(m_{\text{ad}} - m_{\text{u}}) \left( \tanh \left[ \zeta - \frac{r - r_i}{\delta} \right] + \tanh \left[ \frac{r - r_t}{\delta} + \zeta \right] \right), \quad (56)$$

where  $m_{\text{u}} < m_{\text{ad}}$ , and  $\delta$  and  $\zeta$  are parameters controlling the width of the transition. The ambient potential temperature is obtained via its definition,

$$\Theta_a(r) \equiv T_m(r) \left( \frac{\rho_b T_b}{\rho_m(r) T_m(r)} \right)^{1-1/\gamma}. \quad (57)$$

## 10. APPENDIX C: NUMERICAL APPROXIMATIONS

The system of prognostic equations (1)-(3) may be written compactly in Lagrangian formulation

$$\frac{d\mathbf{\Psi}}{dt} = \mathbf{R}, \quad (58)$$

where  $\mathbf{\Psi} = \{\mathbf{u}, \Theta', \mathbf{B}\}$  denotes the vector of prognosed dependent variables and  $\mathbf{R} = \{\mathbf{R}_{\mathbf{u}}, R_{\Theta'}, \mathbf{R}_{\mathbf{B}}\}$  represents the associate forcings on the right-hand-side of (1)-(3). Equations (58), or their conservative counterparts, are integrated in time and space using the non-oscillatory forward-in-time algorithm

$$\mathbf{\Psi}_{\mathbf{i}}^n = \mathcal{L}E_{\mathbf{i}}(\widehat{\mathbf{\Psi}}) + \delta_h t \mathbf{R}_{\mathbf{i}}^n, \quad (59)$$

where  $\widehat{\mathbf{\Psi}} = \mathbf{\Psi}^{n-1} + \delta_h t \mathbf{R}^{n-1}$ ,  $\mathcal{L}E$  symbolizes a two-time-level, optionally semi-Lagrangian or flux-form Eulerian advection operator, respectively, with  $\delta_h t = 0.5\delta t$ . Here,  $\mathbf{\Psi}_{\mathbf{i}}^n$  denotes the solution sought at the mesh point  $(t^n, \mathbf{x}_{\mathbf{i}})$ , and  $t^n = t^{n-1} + \delta t$ . In the context of global MHD experiments of solar convection the MPDATA advection algorithm is used for  $\mathcal{L}E$  (Ghizaru et al. 2010). While the geometric factors arising from the spherical geometry are taken into account in the analysis of sections 4 and 5, for simplicity here we discuss the Cartesian form of the entropy and momentum equations solved by EULAG-MHD; we refer the reader to Smolarkiewicz & Charbonneau (2013) for a detailed exposition of the coordinate dependent form of the model algorithm, and for a description of the geometric factors arising from the use of spherical coordinates.

### 10.1. Entropy equation

The solution to (2) may now be expressed as

$$\Theta_{\mathbf{i}}^n = \mathcal{L}E_{\mathbf{i}}(\widehat{\Theta}) + \delta_h t R_{\Theta, \mathbf{i}}^n, \quad (60)$$

with  $\widehat{\Theta} = \Theta^{n-1} + \delta_h t R_{\Theta}^{n-1}$ . The first term on the rhs of (2) is treated to second-order accuracy, whereas radiative diffusion and Newtonian cooling are treated explicitly to the first order by reproducing the Euler forward structure in the argument of  $\mathcal{L}E$ , which leads to

$$R_{\Theta}^{n-1} \equiv -\mathbf{u}^{n-1} \cdot \nabla \Theta_a + 2\mathcal{H}(\Theta')^{n-1} - 2\alpha \Theta'^{n-1}, \quad (61)$$

and

$$R_{\Theta}^n \equiv -\mathbf{u}^n \cdot \nabla \Theta_a. \quad (62)$$

Equivalently, since

$$\begin{aligned} \mathcal{L}E_{\mathbf{i}}(\widehat{\Theta}) - (\Theta_{\mathbf{i}}^{n-1} + \delta_h t R_{\Theta, \mathbf{i}}^{n-1}) \\ \equiv -\delta t \rho_{\circ}^{-1} \nabla \cdot (\rho_{\circ} \mathbf{u} \widehat{\Theta})_{\mathbf{i}} \\ \approx -\rho_{\circ}^{-1} \int_{t^{n-1}}^{t^n} \nabla \cdot (\rho_{\circ} \mathbf{u} \widehat{\Theta}) dt, \end{aligned} \quad (63)$$

where  $\overline{(\cdot)}$  represents an effective time average over time-step  $\delta t$ . Equation (60) may be rewritten as

$$\Theta_{\mathbf{i}}^n = \Theta_{\mathbf{i}}^{n-1} + \delta_h t R_{\Theta, \mathbf{i}}^{n-1} - \delta t \frac{1}{\rho_{\circ}} \nabla \cdot (\rho_{\circ} \mathbf{u} \widehat{\Theta})_{\mathbf{i}} + \delta_h t R_{\Theta, \mathbf{i}}^n. \quad (64)$$

whereupon substitution of (61) and (62) into (64) gives

$$\begin{aligned} \Theta^n - \Theta^{n-1} = -\delta t \frac{1}{\rho_{\circ}} \nabla \cdot (\rho_{\circ} \mathbf{u} \widehat{\Theta}) \\ - \delta_h t (\mathbf{u}^n \cdot \nabla \Theta_a + \mathbf{u}^{n-1} \cdot \nabla \Theta_a) \\ + \delta t \mathcal{H}(\Theta')^{n-1} - \delta t \alpha \Theta'^{n-1}, \end{aligned} \quad (65)$$

$$(66)$$

where we have omitted the subscript  $\mathbf{i}$  for clarity. It is convenient to label each term in (66) according to

$$S_a \equiv \delta t^{-1} (\Theta^n - \Theta^{n-1}) \quad (67)$$

$$S_b \equiv -\frac{1}{\rho_{\circ}} \nabla \cdot (\rho_{\circ} \mathbf{u} \widehat{\Theta}), \quad (68)$$

$$S_c \equiv -\frac{1}{2} (\mathbf{u}^n \cdot \nabla \Theta_a + \mathbf{u}^{n-1} \cdot \nabla \Theta_a), \quad (69)$$

$$S_d \equiv \mathcal{H}(\Theta')^{n-1} \quad (70)$$

$$S_e \equiv -\alpha \Theta'^{n-1}. \quad (71)$$

The analysis of each term reveals that advection and Newtonian cooling constitute the dominant contributions to the right-hand-side of (66), with radiative diffusion being smaller by at least two orders of magnitude compared to those two. Terms (68) and (69) may therefore be combined to express the first term on the rhs of (18) as

$$-\frac{1}{\rho_{\circ}} \nabla \cdot (\mathbf{F}_{\Theta}) \equiv S_b + S_c, \quad (72)$$

where  $\mathbf{F}_{\Theta}$  stands as a full potential temperature flux representing the contributions from perturbations ( $S_b$ ) and the ambient state ( $S_c$ ).

### 10.2. Momentum equation

The solution to the momentum equation (1) takes the form

$$\mathbf{u}_{\mathbf{i}}^n = \mathcal{L}E_{\mathbf{i}}(\widehat{\mathbf{u}}) + \delta_h t \mathbf{R}_{\mathbf{u}, \mathbf{i}}^n \quad (73)$$

where  $\widehat{\mathbf{u}} = \mathbf{u}^{n-1} + \delta_h t \mathbf{R}_{\mathbf{u}}^{n-1}$  and

$$\mathbf{R}_{\mathbf{u}, \mathbf{i}}^n = \left( \frac{1}{\mu \rho_{\circ}} \mathbf{B} \cdot \nabla \mathbf{B} \right)_{\mathbf{i}}^n - \left[ \mathbf{g}_{\Theta'}^n - 2\mathbf{u} \times \boldsymbol{\Omega} \right]_{\mathbf{i}}^n - (\nabla \varphi')_{\mathbf{i}}^n. \quad (74)$$

The total forcing (74) can be decomposed into contributions from buoyancy, Coriolis and pressure gradient

forces and magnetic tension according to

$$\mathbf{R}_g^n \equiv - \left[ \mathbf{g} \frac{\Theta'}{\Theta_o} \right]_{\mathbf{i}}^n, \quad (75)$$

$$\mathbf{R}_c^n \equiv \left[ 2\mathbf{u} \times \boldsymbol{\Omega} \right]_{\mathbf{i}}^n, \quad (76)$$

$$\mathbf{R}_\varphi^n \equiv -(\nabla \varphi')_{\mathbf{i}}^n, \quad (77)$$

$$\mathbf{R}_t^n \equiv \left( \frac{1}{\mu \rho_o} \mathbf{B} \cdot \nabla \mathbf{B} \right)_{\mathbf{i}}^n. \quad (78)$$

Furthermore, we have

$$\mathcal{L}E_{\mathbf{i}}(\hat{\mathbf{u}}) - \hat{\mathbf{u}}_{\mathbf{i}} = -\delta t \left[ \frac{1}{\rho_o} \overline{\nabla \cdot \rho_o \mathbf{u} \hat{\mathbf{u}}} \right]_{\mathbf{i}}, \quad (79)$$

whereupon (73) may be written as

$$\begin{aligned} \mathbf{u}_{\mathbf{i}}^n - \mathbf{u}_{\mathbf{i}}^{n-1} = & -\delta t \left[ \frac{1}{\rho_o} \overline{\nabla \cdot \rho_o \mathbf{u} \hat{\mathbf{u}}} \right]_{\mathbf{i}} \\ & + \delta_h t (\mathbf{R}_\varphi^n + \mathbf{R}_\varphi^{n-1})_{\mathbf{i}} \\ & + \delta_h t (\mathbf{R}_g^n + \mathbf{R}_g^{n-1})_{\mathbf{i}} \\ & + \delta_h t (\mathbf{R}_c^n + \mathbf{R}_c^{n-1})_{\mathbf{i}} \\ & + \delta_h t (\mathbf{R}_t^n + \mathbf{R}_t^{n-1})_{\mathbf{i}}. \end{aligned} \quad (80)$$

We shall adopt the following notation

$$\mathbf{F}_a \equiv -\overline{\nabla \cdot \rho_o \mathbf{u} \hat{\mathbf{u}}}, \quad (81)$$

$$\mathbf{F}_g \equiv \frac{1}{2} \rho_o (\mathbf{R}_g^n + \mathbf{R}_g^{n-1}), \quad (82)$$

$$\mathbf{F}_\varphi \equiv \frac{1}{2} \rho_o (\mathbf{R}_\varphi^n + \mathbf{R}_\varphi^{n-1}), \quad (83)$$

$$\mathbf{F}_c \equiv \frac{1}{2} \rho_o (\mathbf{R}_c^n + \mathbf{R}_c^{n-1}), \quad (84)$$

$$\mathbf{F}_t \equiv \frac{1}{2} \rho_o (\mathbf{R}_t^n + \mathbf{R}_t^{n-1}), \quad (85)$$

whereby we may express (80) as

$$\frac{\partial \rho_o \mathbf{u}}{\partial t} = \mathbf{F}_a + \mathbf{F}_\varphi + \mathbf{F}_g + \mathbf{F}_c + \mathbf{F}_t. \quad (86)$$

## 11. APPENDIX D

Using the anelastic mass continuity equation (4) and decomposing  $\Theta \equiv \Theta_a + \Theta'$  into the ambient state and its perturbation to rewrite the flux divergence in (20) and (21) gives

$$\begin{aligned} \int_{\partial\Omega} \nabla \cdot (\rho_o \mathbf{u} \Theta) d\sigma &= \int_{\partial\Omega} \rho_o \left( \mathbf{u} \cdot \nabla \Theta' + u_r \frac{\partial \Theta_a}{\partial r} \right) d\sigma \\ &= \int_{\partial\Omega} \rho_o \mathbf{u} \cdot \nabla \Theta' d\sigma \\ &+ \frac{\partial \Theta_a}{\partial r} \int_{\partial\Omega} \rho_o u_r d\sigma, \end{aligned} \quad (87)$$

where we have used the fact  $\Theta_a$  is spherically symmetric when going from the first to the second equality. Since the surface average of the radial mass flux must vanish in the presence of impermeable boundaries (cf. appendix A), the second term on the rhs of the second equality in (87) disappears and we have

$$\begin{aligned} \int_{\partial\Omega} \nabla \cdot (\rho_o \mathbf{u} \Theta) &= \int_{\partial\Omega} \rho_o \mathbf{u} \cdot \nabla \Theta' d\sigma \\ &= \int_{\partial\Omega} \left( \rho_o \mathbf{u}_H \cdot \nabla_H \Theta' + \rho_o u_r \frac{\partial \Theta'}{\partial r} \right) d\sigma \\ &= \int_{\partial\Omega} \left( \nabla_H \cdot (\rho_o \mathbf{u}_H \Theta') - \Theta' \nabla_H \cdot (\rho_o \mathbf{u}_H) \right. \\ &\quad \left. + \rho_o u_r \frac{\partial \Theta'}{\partial r} \right) d\sigma \\ &= \int_{\partial\Omega} \rho_o u_r \frac{\partial \Theta'}{\partial r} + \int_{\partial\Omega} \Theta' \frac{\partial \rho_o u_r}{\partial r} d\sigma. \end{aligned} \quad (88)$$

where  $\mathbf{u}_H$  and  $\nabla_H$  denote the horizontal components of the velocity and gradient operator, respectively. In going from the third to the fourth equality in (88), we used the fact that the surface integral of a horizontal divergence vanishes and (4) to express the divergence of horizontal momentum as a function of radial momentum.

## REFERENCES

- Augustson, K., Brun, A. S., Miesch, M., & Toomre, J. 2015, *ApJ*, 809, 149  
 Antia, H. M. 2003, *ApJ*, 590, 567  
 Beaudoin, P., Charbonneau, P., Racine, E., & Smolarkiewicz, P. K. 2013, *Sol. Phys.*, 282, 335  
 Beaudoin, P., Simard, C., Cossette, J.-F., & Charbonneau, P. 2016, *ApJ*, 826, 138  
 Bhatnagar, A., Jain, K., & Tripathy, S. C. 1999, *ApJ*, 521, 885  
 Brown, B. P., Miesch, M. S., Browning, M. K., Brun, A. S., & Toomre, J. 2011, *ApJ*, 731, 69  
 Brun, A. S., & Toomre, J. 2002, *ApJ*, 570, 865  
 Brun, A. S., Miesch, M. S., & Toomre, J. 2004, *ApJ*, 614, 1073  
 Brummell, N. H., Hurlburt, N. E., & Toomre, J. 1996, *ApJ*, 473, 494  
 Cattaneo, F., Brummell, N. H., Toomre, J., Malagoli, A., & Hurlburt, N. E. 1991, *ApJ*, 370, 282  
 Chaplin, W. J., Appourchaux, T., Elsworth, Y., Isaak, G. R., & New, R. 2001, *MNRAS*, 324, 910  
 Charbonneau, P. 2013, *Solar and Stellar Dynamos* (Springer)  
 Christensen-Dalsgaard, J., Dappen, W., Ajukov, S. V., et al. 1996, *Science*, 272, 1286  
 Cossette, J.-F., Charbonneau, P., & Smolarkiewicz, P. K. 2013, *ApJ*, 777, L29  
 Cossette, J.-F., & Rast, M.P. 2016, *ApJ*, 829, L17  
 Duarte, L.D.V., Wicht, J., Browning, M.K., & Gastine, T. 2016, *MNRAS*, 456, 1708  
 Domaradzki, J.A., Xiao, Z. & Smolarkiewicz, P.K. 2003, *Phys. Fluids*, 15, 3890  
 Elliott, J. R., & Smolarkiewicz, P. K. 2002, *International Journal for Numerical Methods in Fluids*, 39, 855  
 Emilio, M., Kuhn, J. R., Bush, R. I., & Scherrer, P. 2000, *ApJ*, 543, 1007  
 Fan, Y., & Fang, F. 2014, *ApJ*, 789, 35  
 Farhat, A., Jolly, M. S., Titi, E. S. 2015, *Physica D*, 303, 59  
 Farhat, A., Lunasin, E., Titi, E. S. 2016, *J. Math. Anal. Appl.* 438, 492  
 Featherstone, N. A., & Hindman, B. W. 2016, *ApJ*, 818, 32  
 Fletcher, S. T., Broomhall, A.-M., Salabert, D., et al. 2010, *ApJ*, 718, L19  
 Foukal, P. 1987, *J. Geophys. Res.*, 92, 801  
 Foukal, P., Fröhlich, C., Spruit, H., & Wigley, T. M. L. 2006, *Nature*, 443, 161  
 Ghizaru, M., Charbonneau, P., & Smolarkiewicz, P. K. 2010, *ApJ*, 715, L133  
 Grabowski, W. W., & Smolarkiewicz, P. K. 2002, *Monthly Weather Review*, 130, 939

- Gray, D. F., & Livingston, W. C. 1997, *ApJ*, 474, 802
- Guerrero, G., Smolarkiewicz, P. K., Kosovichev, A. G., & Mansour, N. N. 2013, *ApJ*, 779, 176
- Guerrero, G., Smolarkiewicz, P. K., e Gouveia Dal Pino, E.M., Kosovichev, A.G., & Mansour, N.N. 2016, *ApJ*, 819, 104
- Held, I. M. & Suarez, M. J. 1994, *Bull. Amer. Meteor. Soc.*, 75, 1825.
- Käpylä, P. J., Korpi, M. J., Brandenburg, A., Mitra, D., & Tavakol, R. 2010, *Astronomische Nachrichten*, 331, 73
- Käpylä, P. J., Mantere, M. J., & Brandenburg, A. 2012, *ApJ*, 755, L22
- Käpylä, P. J., Mantere, M. J., Cole, E., Warnecke, J., & Brandenburg, A. 2013, *ApJ*, 778, 41
- Krener, A. J., 1980, *IEEE Trans. Automat. Contr.*, 25, 291
- Kuhn, J. R., Bush, R. I., Emilio, M., & Scherrer, P. H. 2004, *ApJ*, 613, 1241
- Li, L. H., Basu, S., Sofia, S., et al. 2003, *ApJ*, 591, 1267
- Libbrecht, K. G., & Woodard, M. F. 1990, *Nature*, 345, 779
- Lipps, F. B., & Hemler, R. S. 1982, *Journal of Atmospheric Sciences*, 39, 2192
- Livingston, W., & Wallace, L. 2003, *Sol. Phys.*, 212, 227
- Margolin, L. G., Smolarkiewicz, P. K. & Wyszogrodzki, A. A. 2006, *J. Appl. Mech.*, 73, 469.
- Masada, Y., Yamada, K., & Kageyama, A. 2013, *ApJ*, 778, 11
- Miesch, M. S., Brun, A. S., De Rosa, M. L., & Toomre, J. 2008, *ApJ*, 673, 557
- Miesch, M. S. 2005, *Living Reviews in Solar Physics*, 2, 1
- Miesch, M. S., Elliott, J. R., Toomre, J., et al. 2000, *ApJ*, 532, 593
- Miesch, M. S., Brun, A. S., & Toomre, J. 2006, *ApJ*, 641, 618
- Nelson, N. J., Brown, B. P., Brun, A. S., Miesch, M. S., & Toomre, J. 2013, *ApJ*, 762, 73
- Nordlund, Å., Stein, R. F., & Asplund, M. 2009, *Living Reviews in Solar Physics*, 6, 2
- Pal, P. S., Singh, H. P., Chan, K. L., & Srivastava, M. P. 2007, *Ap&SS*, 307, 399
- Passos, D., & Charbonneau, P. 2014, *A&A*, 568, A113
- Piotrowski, Z. P., Smolarkiewicz, P. K., S.P. Malinowski, S. P., & Wyszogrodzki, A. A. 2009, *Journal of Computational Physics*, 228, 6268
- Porter, D. H., & Woodward, P. R. 2000, *ApJS*, 127, 159
- Prusa, J. M., Smolarkiewicz, P. K., & Wyszogrodzki, A. A. 2008, *Comput. Fluids*, 37, 1193
- Racine, É., Charbonneau, P., Ghizaru, M., Bouchat, A., & Smolarkiewicz, P. K. 2011, *ApJ*, 735, 46
- Rast, M. P., Ortiz, A., & Meisner, R. W. 2008, *ApJ*, 673, 1209
- Rieutord, M., & Zahn, J.-P. 1995, *A&A*, 296, 127
- Rozelot, J. P., Lefebvre, S., Pireaux, S., & Ajabshirizadeh, A. 2004, *Sol. Phys.*, 224, 229
- Smolarkiewicz, P. K., Kühnlein, C. & Wedi, N. P. 2014, *Journal of Computational Physics*, 263, 185
- Smolarkiewicz, P. K., & Charbonneau, P. 2013, *Journal of Computational Physics*, 236, 608
- Smolarkiewicz, P. K. 2006, *International Journal for Numerical Methods in Fluids*, 50, 1123
- Smolarkiewicz, P. K., Margolin, L. G., & Wyszogrodzki, A. A. 2001, *Journal of Atmospheric Sciences*, 58, 349
- Smolarkiewicz, P. K., & Prusa, J. M. 2002, *International Journal for Numerical Methods in Fluids*, 39, 799
- Sofia, S., & Li, L. H. 2006, *Mem. S. A. It.*, 76, 768
- Spruit, H. C. 1977, *A&A*, 55, 151
- Spruit, H. 1997, *Mem. Soc. Astron. Italiana*, 68, 397
- Spruit, H. 2000, *Space Sci. Rev.*, 94, 113
- Stein, R. F., & Nordlund, A. 1989, *ApJ*, 342, L95
- Stix, M. 1981, *A&A*, 93, 339
- Strugarek, A., Beaudoin, P., Brun, A. S., et al. 2016, *Advances in Space Research*, 58, 1538
- Thompson, M. J., Christensen-Dalsgaard, J., Miesch, M. S., & Toomre, J. 2003, *ARA&A*, 41, 599
- Thuillier, G., Sofia, S., & Haberleiter, M. 2005, *Advances in Space Research*, 35, 329
- Waite, M. L., & Smolarkiewicz, P. K. 2008, *J. Fluid. Mech.*, 606, 239
- Warn-Varnas, A., Hawkins, J., Smolarkiewicz, P. K., et al. 2007, *Ocean Modelling*, 18, 97
- Woodard, M. F. 1987, *Sol. Phys.*, 114, 21
- Woodard, M. F., & Libbrecht, K. G. 2003, *Sol. Phys.*, 212, 51
- Woodard, M. F., & Noyes, R. W. 1985, *Nature*, 318, 449
- Yadav, R. K., Gastine, T., Christensen, U. R., & Duarte, L. D. V. 2013, *ApJ*, 774, 6